ADAR1 Regulates Lipid Remodeling through MDM2 to Dictate Ferroptosis Sensitivity

Che-Pei Kung[1], Nick D. Terzich[2], Ma Xenia G. Ilagen[3,4], Michael J. Prinsen[3], Madhurima Kaushal[5], Raleigh D. Kladney[1], Jade H. Weber[1], Alex R. Mabry[1,6], Luisangely Soto Torres[1,6], Emily R. Bramel[1], Eric C. Freeman[1], Thwisha Sabloak[1], Kyle A. Cottrell[1], Sua Ryu[1], William M. Weber[1], Leonard Maggi Jr.[1], Leah P. Shriver[2,7], Gary J. Patti[2,8,9] and Jason D. Weber[1,4,9,10]

[1]Department of Medicine, Division of Molecular Oncology, Washington University School of Medicine, Saint Louis, MO, USA

[2]Department of Chemistry, Washington University, St. Louis, MO, USA

[3]High Throughput Screening Center, Washington University School of Medicine, Saint Louis, MO, USA

[4]Department of Biochemistry and Molecular Biophysics, Washington University School of Medicine, Saint Louis, MO, USA

[5]Institute for Informatics, Data Science and Biostatistics, Washington University School of Medicine, Saint Louis, MO, USA

[6]Cancer Biology Graduate Program, Washington University School of Medicine, Saint Louis, Missouri, USA

[7]Department of Medicine, Division of Nutritional Science and Obesity Medicine, Washington University School of Medicine, Saint Louis, MO, USA

[8]Department of Genetics, Washington University, St. Louis, MO, USA

[9]Siteman Cancer Center, Washington University, St. Louis, MO, USA

[10]Department of Cell Biology and Physiology, Washington University School of Medicine, Saint Louis, MO, USA

Running title: ADAR1-mediated ferroptosis resistance in triple-negative breast cancer

Co-correspondence:
Che-Pei Kung, Ph.D.
Department of Medicine, Division of Molecular Oncology

Washington University School of Medicine
660 South Euclid Avenue
Campus Box 8069
St. Louis, MO 63110 USA
Email: patkung@wustl.edu
Telephone: 314-747-3898
Fax: 314-362-0152

and

Jason D. Weber, Ph.D.
Department of Medicine, Division of Molecular Oncology
Department of Cell Biology and Physiology

Washington University School of Medicine
660 South Euclid Avenue
Campus Box 8069
St. Louis, MO 63110 USA
Email: jweber@wustl.edu
Telephone: 314-747-3896
Fax: 314-362-0152

Abstract

Triple-negative breast cancer (TNBC), lacking expression of estrogen, progesterone, and HER2 receptors, is aggressive and lacks targeted treatment options. An RNA editing enzyme, adenosine deaminase acting on RNA 1 (ADAR1), has been shown to play important roles in TNBC tumorigenesis. We posit that ADAR1 functions as a homeostatic factor protecting TNBC from internal and external pressure, including metabolic stress. We tested the hypothesis that the iron-dependent cell death pathway, ferroptosis, is a ADAR1-protected metabolic vulnerability in TNBC by showing that ADAR1 knockdown sensitizes TNBC cells to GPX4 inhibitors. By performing single-reaction monitoring-based liquid chromatography coupled to mass spectrometry (LC-MS) to measure intracellular lipid contents, we showed that ADAR1 loss increased the abundance of polyunsaturated fatty acid phospholipids (PUFA-PL), of which peroxidation is the primary driver of ferroptosis. Transcriptomic analyses led to the discovery of the proto-oncogene MDM2 contributing to the lipid remodeling in TNBC upon ADAR1 loss. A phenotypic drug screen using a ferroptosis-focused library was performed to identify FDA-approved cobimetinib as a drug-repurposing candidate to synergize with ADAR1 loss to suppress TNBC tumorigenesis. By demonstrating that ADAR1 regulates the metabolic fitness of TNBC through desensitizing ferroptosis, we aim to leverage this metabolic vulnerability to inform basic, pre-clinical, and clinical studies to develop novel therapeutic strategies for TNBC.

Introduction

Triple-negative breast cancer (TNBC), defined by the lack of estrogen receptor (ER), progesterone receptor (PR) and HER2 expression, accounts for about 15 percent of all breast cancer diagnoses in the United States each year[1]. Despite recent development of PARP inhibitors, immunotherapy and antibody-drug conjugates, there remains a significant gap for targeted therapies against TNBC[2]. It leaves surgery, radiation and chemotherapy as the main treatment options, leading to generally poor prognosis. A multi-prong approach to investigate the immunogenic, epigenetic and metabolic landscapes of TNBC as well as its tumor microenvironment (TME) is underway to identify points of vulnerability to develop novel and effective therapies[3-5].

One such vulnerability is iron-mediated cell death, or ferroptosis. Ferroptosis is a distinctive form of programmed cell death depending on iron-mediated peroxidation of long polyunsaturated fatty acids (PUFA) to incorporate into and break down cell membranes[6]. TNBC cells have been found to be sensitive to ferroptosis through multiple mechanisms. TNBC cell lines have been found to be glutamine auxotrophs, resulting in increased levels of environmental cystine acquisition and heightened sensitivity to inhibition of the glutamate/cystine antiporter xCT[7]. The xCT-cystine axis operates upstream of glutathione, which counters oxidative stress through its antioxidant activity. It has been shown that cellular levels of glutathione are lower in TNBC cell lines, rendering them more vulnerable to ferroptosis inducers that function through inhibiting GPX4, the catalyzer of glutathione's antioxidant function[8,9]. Dysregulation of iron metabolism has also been noted in TNBC, expressing lower levels of iron exporter ferroportin leading to increased cellular labile iron pools[9,10]. Moreover, a subset of TNBC cell lines expressed higher level of ACSL4, which activates long-chain PUFA for phospholipid

biosynthesis to enrich cellular membranes[11]. It has been suggested that TNBC's levels of sensitivity to ferroptosis are correlated with abundance of specific PUFA species, partially dictated by expression levels of enzymes contributing to PUFA biosynthesis, such as Acyl-CoA synthetase long-chain family member 1 (ACSL1) and fatty acid desaturases 1 and 2 (FADS1/2)[12,13].

Adenosine Deaminase Acting on RNA (ADAR1, encoded by *ADAR*) can convert adenosine to inosine within cellular dsRNA, in a process known as A-to-I editing. Elevated expression of ADAR1 is prevalent in breast cancer and ADAR1-mediated A-to-I editing has been shown to contribute to tumor progression and therapy resistance in breast cancer, including TNBC[14-18]. We have previous reported a TNBC-centric ADAR1 dependency phenomenon, in which ADAR1 protects TNBC cells from translational stress and type I interferon (IFN) activation predisposed by TNBC cells' elevated level of interferon stimulated gene (ISG) signatures[19]. ADAR1-mediated regulation of innate immune response has been noted in several cancer types, and ADAR1 loss has been shown to sensitize cancer cells to immunotherapy[20-23]. Through its ability to prevent cytotoxic inflammatory response, ADAR1 also protects cancer cells from other anti-tumorigenic stresses, such as necroptosis and epigenetic modulation[24,25]. Few studies, however, have investigated ADAR1's ability to regulate cancer cells' metabolic fitness and their sensitivity to metabolic stresses. Considering ADAR1's known role in metabolic regulations and the importance of cancer metabolism, it is important to fill such knowledge gaps[26,27].

In the current study, we demonstrate that ADAR1 protects TNBC cells from ferroptotic cell death through regulating MDM2 expression and lipid profile reprogramming. Our observations indicate broader applications of ADAR1-targeting therapies and open opportunities to repurpose ferroptosis-inducing drugs for synergistic effects against TNBC.

Results

ADAR1 protects TNBC cells from ferroptosis induction

To determine if ADAR1 inhibits ferroptosis directly, we knocked down ADAR1 expression with a short-hairpin RNA (shRNA) in TNBC cell line MDA-MB-231 (**Figure S1A**). The level of malondialdehyde (MDA), a byproduct of lipid peroxidation, was measured to show that cells with ADAR1 knockdown (ADAR1-Deficient cells) did not display increased ferroptosis activity compared to cells transduced with non-targeting shRNA (shNT), or ADAR1-Intact cells (**Figure S1B**). Similarly, by staining both the reduced and oxidized forms of the lipid peroxidation probe BODIPY^{TM} 581/591 C11 to compare their intensity, it was revealed that reduced expression of ADAR1 did not enhance the cells' ability to oxidize polyunsaturated fatty acids (**Figure S1C-D**). To corroborate these observations, cell viability analysis was conducted to show that reduced proliferation and viability of MDA-MB-231 cells resulting from ADAR1 knockdown could be partially rescued by either an apoptosis inhibitor (Z-VAD-FMK) or an eIF2α inhibitor (ISRIB), but not by ferroptosis inhibitors Ferrostatin-1 and Liproxstatin-1 (**Figure S1E**). These results suggest that altering ADAR1 expression does not overtly impact ferroptosis activity in cells.

ADAR1-Intact and ADAR1-Deficient MDA-MB-231 cells then were tested to determine if ADAR1 expression influences cells' sensitivity to ferroptosis induction. Ferroptosis in MDA-MB-231 cells can be induced by GPX4 inhibitor RSL3, whose effect can be rescued by ferroptosis inhibitor Ferrostatin-1 or UAMC, but not Z-VAD-FMK or necroptosis inhibitor Necrostatin-1 (**Figure S1F**). It was first observed that ADAR1-Deficient MDA-MB-231 cells became much more sensitive, compared to ADAR1-Intact cells, to RSL3 at concentrations as low as 50nM (**Figure 1A**). Cell viability assay was performed to determine IC_{50} (half-maximal inhibitory concentration) of RSL3, and ADAR1-Defective cells (IC_{50} = ~0.11μM) were shown to

be more than 25-fold more sensitive compared to ADAR1-Intact cells (IC_{50} = ~2.9μM) (**Figure 1B**). Similar level of sensitization was observed when using another GPX4 inhibitor, ML162, to treat ADAR1-Deficient (IC_{50} = ~0.08μM) and ADAR1-Intact cells (IC_{50} = ~2.27μM) (**Figure 1C**).

To evaluate if this sensitization effect occurs in TNBC cells besides MDA-MB-231, three other TNBC cells lines (MDA-MB-468, MDA-MB-436, HCC1806) were transduced with shNT and shADAR1 before being subjected to RSL3 treatment. In all three TNBC cell lines tested, ADAR1 knockdown resulted in increased sensitivity to RSL3 ranging from 3.5-fold (HCC1806) to over 25-fold (MDA-MB-468) (**Figure 1D-F**). Four non-TNBC cell lines (MCF7, T47D, ZR75.1, SKBR3) were also examined for their sensitivity to RSL3 with or without ADAR1 knockdown. Interestingly, none of the non-TNBC cell lines tested acquired higher sensitivity to RSL3 upon ADAR1 knockdown (**Figure S1G-J**). It indicates that ADAR1 regulates TNBC cell lines' metabolic fitness by protecting them from ferroptosis induction.

An orthotopic implantation mouse model was established to test if these *in vitro* results can be recapitulated *in vivo*. MDA-MB-231 cells stably transduced with Tet-inducible shADAR1 were implanted into the mammary fat pad of female immunocompromised NSG mice (**Figure 1G and 1H**). Upon formation of palpable tumors 10 days post implantation, half of the mice were switched to doxycycline-containing diet to induce expression of shADAR1 to reduce ADAR1 levels (**Figure S1K**). Both control- and doxycycline-diet mice were subjected to i.p. injection of RSL3 (100mg/kg weight; twice a week) for 5 weeks before tumors were resected. Weekly health and weight monitoring suggested no additional toxicity associated with RSL3 treatment (**Figure S1L**). Doxycycline diet or RSL3 treatment alone reduced tumor burdens, and mice that received the combination treatment (doxycycline diet + RSL3) experienced significantly slower tumor

progression (**Figure 1I-K, Figure S1M-O**). Immunohistochemical staining of 4-Hydroxynonenal (4HNE), a product of lipid peroxidation, showed that the combination treatment enhances ferroptosis phenotype in MDA-MB-231-formed mammary tumors (**Figure 1L**). These results suggest that ADAR1 reduction and ferroptosis induction form synergy to suppress tumorigenesis.

Knockdown of ADAR1 leads to lipid remodeling

Multiple pathways contribute to ferroptosis sensitivity, including ferrous iron availability, glutathione activity, and relative abundance of polyunsaturated fatty acid (PUFA) over monounsaturated fatty acid (MUFA)[6] (**Figure 2A**). Focusing on a cell line that can be highly sensitized to ferroptosis induction by ADAR1 knockdown, MDA-MB-231, these elements were evaluated to test the hypothesis that ADAR1-Deficient cells are primed to the cytotoxic effects of ferroptosis induction.

In ADAR1-Defective cells, both the level of total glutathione and ratio between reduced and total glutathione remain the same (**Figure S2A-B**). FerroOrange staining was used to detect ferrous iron (Fe^{2+}) to show that ADAR1-Deficient MDA-MB-231 cells also do not display significantly higher level of ferrous iron (**Figure S2C-D**). It suggests that the elevated sensitivity to ferroptosis cannot be attributed to either alteration of glutathione antioxidant activity or abundance of ferrous iron upon ADAR1 knockdown.

A non-targeted lipidomic analysis was performed to identify potential changes in lipid profiles between ADAR1-Intact and ADAR1-Deficient cells. Interestingly, a clear pattern switch was detected with the species of phosphatidylcholine (PC), the most abundant phospholipid in mammalian cells and the most impactful phospholipid in controlling ferroptosis sensitivity

(**Figure 2B**). The observed lipid reprogramming disproportionally enriched PC species of longer carbon chains with higher degrees of unsaturation indicated by the number of double bonds within the carbon chain (**Figure 2C-F**). Some of the longest and most highly unsaturated PC species, such as PC38:4, are among the most significantly enriched PCs in ADAR1-Defective cells (**Figure 2G, Figure S2E**).

To investigate if similar lipid reprogramming occurs in TNBC cells sensitized by ADAR1 knockdown to a lesser extent, lipidomic analysis was performed to compare between ADAR1-Intact and ADAR1-Deficient MDA-MB-436 cells (**Figure S2F**). Several highly unsaturated PCs, such as PC 34:3, 35:3, and 44:6, were found to be enriched in ADAR1-Deficient MDA-MB-436 cells (**Figure 2H-I**). The enrichment upon ADAR1 knockdown, however, was not limited to PUFA, as some MUFA PC species (i.e. PC36:1, 37:1, 38:1) were also upregulated in ADAR1-Deficient cells. Other PUFA PC species, meanwhile, appeared to be reduced in ADAR1-Deficient cells (**Figure S2G**).

Interestingly, PUFAs of other phospholipid families, such as phosphatidylserine (PS) and phosphatidylethanolamine (PE), were also found to be disproportionally enriched in ADAR1-Deficient MDA-MB-436 cells (**Figure 2J-L**, **Figure S2H-I**). These results showed that ADAR1 reduction leads to lipid reprogramming, specifically enrichment of PUFA over MUFA and saturated fatty acid (SFA). It suggests that in TNBC cells, ADAR1 helps maintaining FA homeostasis favoring MUFA and SFA. Interestingly, expression levels of ADAR1 strongly correlate with abundance of SFA (PC32:0) and MUFA (PC32:1 and PC34:1) species in TNBC, but not non-TNBC, cells according to the publicly available metabolomics dataset (**Figure S2J-L**).

ADAR1 regulates MDM2 expression to dictate lipid profiles and ferroptosis sensitivity

To identify potential mechanisms that contribute to ADAR1-regulated lipid reprogramming in TNBC cells, four TNBC cell lines (MDA-MB-231, MDA-MB-468, HCC1806, BT549) were subjected to RNA-seq analyses to compare transcriptomic profiles between ADAR1-Intact and ADAR1-Deficient cells (**Figure S3A**).

Pathway analyses were performed to provide a glimpse of cellular functions impacted upon ADAR1 knockdown. Genes that were significantly altered in at least three cell lines tested can be categorized into a variety of pathways, including metabolic regulations in cancer cells as well as lipid and fatty acid metabolism (**Figure 3A-D, Figure S3B-C, Table S1-4**). Gene set enrichment analysis (GSEA) with RNA-seq data of MDA-MB-231 cells also suggests that ADAR1 reduction resulted in significant alterations in transcriptomes involved in fatty acid metabolism, but not in glutathione activity, iron metabolism, or direct ferroptosis regulation (**Figure 3E-F, Figure S3D-E**). GSEA results from MDA-MB-231 cells also suggest a lack of clear effect on interferon signaling gene sets, while cell cycle related transcriptome is significantly affected (**Figure S3F-G**). Interestingly, when other metabolic pathways were evaluated, ADAR1 knockdown was found to have no effect on the genet set associated with glycolysis, while significantly alter the transcriptome involved in amino acid metabolism (**Figure S3H-I**). It suggests that ADAR1's ability to regulate metabolic fitness in TNBC might extend beyond lipid programming.

To narrow down genetic targets for further investigation, more stringent cut-offs were applied to identify individual genes that are altered the most between ADAR1-Intact and ADAR1-Deficient cells. Fourteen genes (including *ADAR*, which encodes ADAR1) were downregulated in all four

TNBC cell lines tested, while 4 genes were upregulated (**Figure 3G-H**). Among these genes, *MDM2* has been shown to be subjected to ADAR1-mediated transcriptional regulation[28]. Induction of MDM2 protein level in ADAR1-Deficient cells was confirmed using western blot analysis, and reduced RNA editing at the reported 3'UTR double-stranded editing site was observed using both Sanger sequencing and RNA editing site-specific quantitative PCR (RESS-qPCR) (**Figure 3I-K, Figure S3J-K**).

It was recently shown that MDM2 promotes ferroptosis sensitivity through mediating lipid remodeling, including induction of PUFA levels[29]. To determine if MDM2 is also capable of promoting ferroptosis sensitivity in TNBC cells, MDA-MB-231 cells were stably transfected with a MDM2-overexpressing construct before being subjected to RSL3 treatment (**Figure 3L**). Overexpression of MDM2 is sufficient to sensitize MDA-MB-231 cells to RSL3 treatment, albeit to a lesser degree compared to the effect mediated by ADAR1 knockdown (**Figure 3M**).

To determine if MDM2 promotes enrichment of PUFAs in breast cancer cells, MDA-MB-231 cells overexpressing MDM2 were subjected to untargeted lipidomic analysis. A Tet-inducible MDM2 construct was used in this experiment to identify profiles of PC PUFA at both 48 and 96 hours after doxycycline treatment (**Figure S3L**). At 48 hours post treatment, a few PC PUFAs (i.e. PC34:3) were seen enriched (**Figure S3M**). After 96 hours of MDM2 overexpression, however, a broader enrichment profile of PC PUFAs became prominent, including significant inductions of several highly unsaturated PC species, such as PC42:7 and PC42:8, among others (**Figure 3N-O, Figure S3N**).

To determine if the elevated ferroptosis sensitivity upon ADAR1 reduction can be indeed attributed to MDM2 induction, a rescue experiment was conducted with RSL3-treated ADAR1-

Intact and ADAR1-Deficient MDA-MB-231 cells. The inflection-point concentration of RSL3 (100nM) distinguishing between ADAR1-Intact and ADAR1-Deficient MDA-MB-231 cells was used in combination with MDM2 inhibitors. Cell viability analysis was performed to detect reduced viability in RSL3-treated ADAR1-Deficient cells and effect of MDM2 inhibition. All three MDM2 inhibitors used (MX69, SP-141, MEL23) were shown to partially rescue RSL3-treated ADAR1-Deficient cells (**Figure 3P**). An agonist of peroxisome proliferator-activated receptor alpha (PPAR-α), pirinixic acid, was also shown to confer mild yet significant rescue effect, consistent with the hypothesis that MDM2 promotes ferroptosis sensitivity through suppressing PPAR-α activity[29]. These results collectively indicate that ADAR1 regulates lipid remodeling through MDM2 to protect TNBC cells from ferroptosis induction.

ADAR1 loss synergizes with cobimetinib to suppress tumorigenesis

The most commonly used ferroptosis inducers in preclinical studies, such as RSL3, remain distant from clinical applications due to poor pharmacological profiles and excessive toxicity[30]. Meanwhile, many drugs currently being used in clinics or tested in clinical trials have been shown to possess ferroptosis-inducing activities[31]. The opportunity exists, therefore, to harness the lipid-remodeling effect of ADAR1 inhibition to enhance efficacy of treatments readily available to patients.

To identify drug candidates synergizing with ADAR1 inhibition, a high-throughput screening was conducted. Cell viability analysis was used to assess the effect of ADAR1 status on MDA-MB-231 cells' sensitivity to drugs included in a ferroptosis-focused library (**Figure 4A**). Drugs that synergize with ADAR1 inhibition (ADAR1-sensitized) were expected to suppress ADAR1-Deficient cells more effectively than ADAR1-Intact cells similarly to RSL3, which was used as a positive control in the screening (**Figure 4B-C**).

By comparing the relative viability between ADAR1-Deficient and -Intact cells, several drugs were identified to react at least twice as strong with ADAR1-Deficient MDA-MB-231 cells (**Figure 4D-E**). Siramesine is a lysosome disrupting agent that has been shown to induce ferroptosis by promoting ROS (reactive oxygen species) – mediated oxidative stress and reducing expression of ferroportin-1, an iron transport protein[32,33]. SB590885 is a potent inhibitor of B-Raf, whose inhibition has been shown to induce oxidative stress and accumulation of ROS[34,35]. UC2288 is a derivative of Sorafenib, a known ferroptosis inducer, and has been shown to promote ferroptosis through regulating p21 activity[36,37]. Alpha-Mangostin is a dietary xanthone that has also been shown to induce ROS activity[38]. Considering the effect of ADAR1 reduction on lipid remodeling, however, the synergy might work through compensating α-Mangostin-mediated suppression of lipogenesis[39]. Similar mechanisms might be attributed to the sensitization to Nordihydroguaiaretic acid (NDGA), a natural product inhibitor of 5-lipoxygenase (5-LOX) that promotes the peroxidation of PUFA[40,41]. GW284543 and cobimetinib are both MEK inhibitors, and MEK inhibition has been recently shown to induce ferroptosis in lung and ovarian cancers[42,43].

Among the hits identified, cobimetinib is the only drug clinically available to treat FDA-approved indications, including metastatic melanoma and histiocytic neoplasms[44,45]. Cobimetinib is being evaluated in clinical trials for its efficacy in other cancers and has shown potential to prolong survival of TNBC patients when combined with chemotherapy and immunotherapy[46]. Interestingly, publicly available drug response data show that cobimetinib displays dramatically stronger activity towards TNBC compared to non-TNBC cell lines, similarly to carboplatin that is known to improve TNBC treatment outcome[47] (**Figure S4A-B**).

The orthotopic implantation mouse model described earlier was performed to test the potential synergistic effect between ADAR1 loss and cobimetinib *in vivo* (**Figure S4C**). MDA-MB-231 cells expressing Tet-inducible shADAR1 were implanted into the mammary fat pad of female NSG mice. Upon formation of palpable tumors, mice were fed control or doxycycline-containing diet before being subjected to cobimetinib treatment (oral administration at 20mg/kg weight; twice a week) for 5 weeks before tumors were resected. Weekly health and weight monitoring suggested no additional toxicity associated with cobimetinib treatment (**Figure S4D**). The combination treatment of doxycycline diet and cobimetinib significantly reduce the tumor burden compared to doxycycline diet or cobimetinib alone (**Figure 4F-H, Figure S4E-G**). It indicates a strong synergistic effect between ADAR1 reduction and cobimetinib to suppress tumorigenesis.

Discussion

Justified by data shown in this study, we expanded our knowledge of ADAR1-associated vulnerabilities in TNBC by demonstrating their increased sensitivity to ferroptosis upon ADAR1 loss. Interestingly, two recent studies showed that ADAR1 loss can lead to overt ferroptosis phenotypes, including in breast cancer cells[48,49]. It is unclear what caused the disparate observations. Different elements of experimental methodology, such as cell culture condition, can affect detection of ferroptosis phenotypes[50,51]. Notably, CRISPR (clustered regularly interspaced short palindromic repeats) – mediated gene editing used to reduce ADAR1 expression in these studies has been shown to alter signaling pathways of tumor suppressor p53, which can promote ferroptotic cell death[52,53]. Regardless of the reasons for these inconsistencies, our results agree with the premise that ADAR1 plays a protective role against ferroptosis and represents a novel target to sensitize cancer cells to ferroptosis-promoting agents.

ADAR1-mediated desensitization to ferroptosis was attributed to reprogramming of lipid profiles, as ADAR1 reduction led to increased PUFA abundance and PUFA/MUFA ratio. Transcriptomic analysis revealed protooncogene MDM2 as one of the commonly regulated genes in ADAR1-Deficient TNBC cell lines that are sensitized to ferroptosis. Consistent with its recently identified function in promoting ferroptosis through lipid reprogramming, alterations of expression and activity of MDM2 were shown to connect to ADAR1-regulated ferroptosis sensitivity[29]. Results presented in this manuscript depict a novel mechanism by which ADAR1 protects TNBC cells from stresses that could lead to ferroptosis (**Figure 4I**).

Sensitivity of TNBC cells to all three ferroptosis inducers used in this study (RSL3, ML162, cobimetinib), interestingly, are inversely correlated with their dependency on ADAR1 (**Figure S4H-J**). It suggests the possibility that TNBC cells' dependency on ADAR1 could be attributed to its ability to protect them from ferroptosis induction, akin to the phenomenon of oncogene addiction[54]. Although recent studies questioned ADAR1's status as a *bona fide* oncogene, it undoubtably deserves to be considered a critical non-oncogene target for its ability to suppress multiple stresses directly and indirectly[55,56]. We posit that the induced ferroptosis sensitivity in ADAR1 knockdown TNBC cells is attributed to their intrinsic cellular environment taking advantage of MDM2-facilitated remodeling of PUFA/MUFA ratio upon GPX4 inhibition. The lack of ferroptosis induction with ADAR1 knockdown alone suggests that TNBC cells' lipid profile is not the limiting factor, and the observed lipid remodeling serves as a priming event. Further supporting the potential of this approach, recent studies revealed that TNBC are protected from ferroptosis by MUFAs generated both intracellularly and by their originating environment[57-59].

Preliminary results showed that non-TNBC cell lines are not sensitized to GPX4 inhibitor RSL3 upon ADAR1 knockdown. It will be interesting to investigate if the ADAR1-MDM2-PUFA axis is also altered in these cells without the sensitization effect. It has been shown previously that multiple mechanisms contributing to resistance of ferroptosis are elevated in non-TNBC breast cancer cells, suggesting higher thresholds to sensitize them to ferroptosis inducers[60-64]. It is also worth noting that TNBC disproportionally possess deactivating p53 mutations that abrogate MDM2 interactions[65]. The ability of MDM2 to promote lipid remodeling and ferroptosis sensitivity, therefore, could be dictated by its dynamic relationship with p53. The recent discovery of mutant p53's role in protecting TNBC from ferroptosis indicates that MDM2 might play an antagonistic role in promoting ferroptosis sensitivity in TNBC[66]. Moreover, Adams *et al.* recently suggested that MDM2 is required for p53-inactivated TNBC cell survival[67]. While it is not surprising with MDM2's many p53-independent pro-tumorigenic functions, it signals the need to understand MDM2's complex role in ADAR1-targeting strategy against TNBC[68].

Exciting opportunities are highlighted by the synergistic effect between ADAR1 loss and ferroptosis to identify novel combinatory cancer treatments. Besides the lack of clinically proven ADAR1 and ferroptosis modulators, both ADAR1 inactivation and ferroptosis have been associated with pathological consequences, handicapping the drug development progress[30,69]. In addition to development of effective ADAR1 inhibitors, functional drug repurposing offers a derisking strategy to bring biological insights closer to clinical applications[70,71]. A ferroptosis-focused high-throughput drug screen identified cobimetinib, an FDA-approved MEK inhibitor with ferroptosis-inducing activity, to be sensitized with ADAR1 loss. Cobimetinib and other MEK inhibitors have been shown in both preclinical and clinical settings to inhibit TNBC tumorigenesis[46,72]. In addition to its ability to promote ferroptosis, cobimetinib has been shown

to induce a type I interferon response[73]. It demonstrated the potential of repurposing drugs coordinating with multiple signaling pathways downstream of ADAR1 inhibition to result in superior efficacy against TNBC. It will be interesting to investigate if other existing TNBC treatments, such as platinum-based agents, also synergize with ADAR1 inhibition with their ferroptosis-promoting activity[74].

Raised by the new finding are many questions about the implication of ADAR1's ability to regulate lipid metabolism and ferroptosis sensitivity. Does ADAR1 expression or its editing profile have prognostic value, like recently shown androgen receptor, to predict TNBC patients' response to ferroptosis inducing agents[75]? As both ferroptosis and ADAR1 inhibition can sensitize "immune cold" tumors to immunotherapy, does a sequential or combined approach targeting ADAR1, ferroptosis, and immune check points have the potential to minimize treatment resistance[76,77]? Considering ADAR1's known role in regulating systemic metabolic functions, does it protect TNBC from other metabolic stresses, such as amino acid dysregulation[27]? And how do ADAR1-regulated metabolic adaptations fit into the development of dietary interventions to improve the treatment of cancers, including TNBC[78-80]? Possessing the capability to alter a quarter of the entire RNA species, ADAR1 holds immerse potential for exploitation to develop innovative therapies against tough-to-treat cancers like TNBC.

Materials and Methods

Cell lines, reagents, and plasmids

Breast cancer cell lines (MDA-MB-231, MDA-MB-436, MDA-MB-468, HCC1806, BT549, BT20, MCF7, T47D, ZR751, SKBR3) and human embryonic kidney 293T (HEK293T) cells were obtained from American Tissue Cells Consortium (ATCC, Manassas, VA USA). All cancer

cell lines were maintained in Dulbecco's Modification of Eagle's Medium (DMEM, GE Life Sciences, Pittsburgh, PA USA) supplemented with 10% fetal bovine serum (FBS, Gibco, 10091-148), Sodium Pyruvate (Cellgro, Waltham, MA USA, 30-002-CI), Non-Essential Amino Acids (NEA, Cellgro, 25-030-CI), and L-glutamine (Cellgro, 25-005-CI). Sensitivity of cells to ferroptosis inducing agents were tested in defined medium with low serum using DMEM supplemented with 2% FBS and L-glutamine. LipoFexin (Lamda Biotech, St. Louis, MO USA, TS310) was used to generate lentivirus. Fugene 6 transfection reagent (Promega, E2692) was used for other transfection experiments.

Tetracycline-inducible shADAR1 was generated by cloning shADAR1 oligonucleotides into Tet-pLKO.1-puro construct with AgeI and EcoRI restriction enzyme sites. Tet-inducible MDM2-overexpressing construct was generated by subcloning MDM2 open-reading frame (ORF) from pCMV-myc3-MDM2 (Addgene 20935) into pSBtet-GP sleeping beauty vector (Addgene 60495) using the Sfil restriction enzyme site. pSBtet-GP-MDM2 and pCMV(CAT)T7-SB100 transposase construct (Addgene 34879) were co-transfected into MDA-MB-231 cells to generate a puromycin-resistant stable cell line. Commercially available chemicals and plasmids, as well as primers and oligonucleotides used are listed in the Resources Table.

Lentiviral production and transduction

To generate lentivirus, HEK293T cells were transfected using LipoFexin with pCMV-VSV-G, pCMV-ΔR8.2, and expression constructs (pLKO.1-puromycin backbone for short-hairpin RNAs). Growth medium was replaced with fresh medium 24hr after transfection, and supernatants containing lentivirus were harvested 24hr later. For transduction, one million cells were infected with lentivirus for 24hr in the presence of 10 µg/ml protamine sulfate to facilitate

viral entry. Transduced cells were selected with puromycin (2 µg/ml) for at least 72hr. Sequences of shRNAs are listed in the Resource table.

Cell viability assay

For cell viability assays, cells were plated at a density of 1,000 to 3,000 cells per well on a 96-well plate and left to grow overnight in complete growth medium at 37°C. Cells were then treated with the indicated drugs in equal volume at 2× desired concentration and left to incubate for 72 h. Cells were then incubated with CellTiter-Glo® 2.0 Reagent (Promega, Madison, WI, USA, G924C) for 1h at room temperature, and viability was read out according to the manufacturer's protocol on a GloMax Navigator Microplate Luminometer (Promega, GM2000). The half-maximal inhibitory concentration (IC_{50}) was determined using a nonlinear regression model using Prism 10 software (GraphPad).

Lipid peroxidation assay; Glutathione activity assay; Ferrous iron assay

Biochemical assays were performed to evaluate ferroptosis phenotypes or molecular mechanisms contributing to cells' sensitivity to ferroptosis induction. Level of lipid peroxidation was determined by 1) measuring its natural byproduct malondialdehyde (MDA) using MDA Colorimetric/Fluorometric Assay (Abcam, Cambridge, UK, ab118970), or by 2) staining and comparing levels of reduced and oxidized forms of lipid peroxidation probe BODIPY™ 581/591 C11 (Image-iT™ Lipid Peroxidation Kit, Thermo Fisher Scientific, Waltham, MA USA), according to manufacturer's instruction. Intracellular oxidative stress level was determined by measuring the ratio between reduced (GSH) and oxidized (GSSG) forms of Glutathione using GSH/GSSG Ratio Detection Assay (Abcam, ab205811) according to manufacturer's instruction. Ferrous iron, which drives ferroptosis, was measured by FerroOrange staining (Dojindo, Japan,

F374) according to the manufacturer's instructions. Quantification of signal intensity was performed using ImageJ software (NIH, Bethesda, MD USA).

Untargeted lipidomic analysis with reversed-phase liquid chromatography (RPLC)

Cells were washed with cold PBS 3 times, cold molecular biology grade water (Corning, Glendale, AZ, 46-000-CM) 3 times, metabolically quenched with cold methanol for 5 min, scraped harvested, and centrifuged at 10,000 × g for 5 min to remove supernatant. Pellets were dried using CentriVap Concentrator (Labconco, Kansas City, MO, 79700-00) and stored in -80°C before extraction of metabolites. Cold extraction buffer containing Methanol:Acetonitrile:Water at 2:2:1 ratio was added to the pellets. Samples were then subjected to 3 times of 30-sec vortex → 1-min liquid nitrogen bath → 10-sec thaw → 10-min bath sonication at 25°C (Fischer Scientific, CPXH Series Model 3800 Heated Ultrasonic Cleaner), before being stored at -20°C for 2 hours to overnight. After centrifuging at 14000 RPM at 4°C for 10 min, sample supernatants were transferred to new Eppendorf tubes and speed dried for 2 hours. BCA Protein Assay was performed on cell pellets in advance to determine protein concentration. Isopropanol:Methanol at 1:1 ratio was added at 1µL per 2.5µg of proteins to the residue and subjected to 2 times of 5-min bath sonication at 25°C → 1-min vortex, before being stored at 4°C for 1 hour to overnight. After centrifuging at 14000 RPM at 4°C for 10 min, supernatants were transferred to LC vials for LC/MS analysis.

No plastics were used to minimize palmitate contamination. An aliquot (4µL) of the extracted sample was injected onto a Waters HSS T3 1.8µM, 2.1x150mm column with a 1.8µM, 2.1x50mm guard column connected to 1290 Infinity II LC. The columns were used with the following buffers and gradients: Mobile Phase A = 40% water, 60% Acetonitrile, 0.1% Formic

Acid, 10mM Ammonium Formate, 2.5µM Medronic Acid; Mobile Phase B = 90% Isopropanol, 10% Acetonitrile, 0.1% Formic Acid, 10mM Ammonium Formate; Needle Wash = 70% Mobile Phase A solution + 30% Mobile Phase B solution; Seal Wash = 9:1 Water:Isopropanol. All solutions were mixed and degassed for 10 min before use. The binary pump was operated at 70% A + 30% B from 0 - 17 min, 25% A + 75% B 0% B from 17 - 20 min, 15% A + 85% B from 20 - 23 min, 100% B from 23 - 27 min, and 70% A + 30% B thereafter at constant 0.25 mL/min flow rate. MS detection was carried out using Agilent 6545 Q-TOF with 150-1,200 Da mass range. An internal standard sample (Avanti Research, SPLASH® LIPIDOMIX® Mass Spec Standard, 330707) was used to normalize for injection variability. Lipid Annotator (Agilent) was used to generate a target list for all lipids detected, and DecolD was used to identify polar lipids[81].

Bulk RNA sequencing and analysis

Total RNA was isolated from cells using miRNeasy Mini Kit (Qiagen, Hilden, Germany, 217004) including on-column DNase digestion following the manufacturer's protocol. Samples were prepared according to RiboErase library kit (Roche) manufacturer's protocol, indexed, pooled, and sequenced on an Illumina NovaSeq S4. Base calls and demultiplexing were performed with Illumina's bcl2fastq software and a custom python demultiplexing program with a maximum of one mismatch in the indexing read. RNA-seq reads were then aligned to the Ensembl release 76 primary assembly with STAR version 2.5.1a1. Gene counts were derived from the number of uniquely aligned unambiguous reads by Subread:featureCount version 1.4.6-p52. Sequencing performance was assessed for the total number of aligned reads, total number of uniquely aligned reads, and features detected. All gene counts were then imported into the R/Bioconductor package EdgeR and TMM normalization size factors were calculated to adjust

for samples for differences in library size. Ribosomal genes and genes not expressed in the smallest group size minus one sample greater than one count-per-million were excluded from further analysis. The TMM size factors and the matrix of counts were then imported into the R/Bioconductor package Limma. Weighted likelihoods based on the observed mean-variance relationship of every gene and sample were then calculated for all samples with the voomWithQualityWeights. The performance of all genes was assessed with plots of the residual standard deviation of every gene to their average log-count with a robustly fitted trend line of the residuals. Differential expression analysis was then performed to analyze for differences between conditions and raw p-values and Benjamini-Hochberg false-discovery rate adjusted p-values were determined to filter results based on cut-off. Biological and functional pathways analyses, as well as gene set enrichment analyses were performed with the Enrichr platform, the GeneOntology enrichment tools, and the Gene Set Enrichment Analysis (GSEA) software[82-87].

Immunoblotting analysis

Cell lysates were extracted from cells at ~90% confluence. Cells were washed with phosphate-buffered saline (PBS, GE Life Sciences), scrape harvested, centrifuged at 1000 × g for 5 min, and lysed with RIPA buffer (20mM Tris-HCl pH7.5, 150mM NaCl, 1mM EDTA, 1% NP-40, 0.1% SDS, 0.1% Deoxycholate) supplemented with 10mM PMSF and HALT protease inhibitor cocktail (Thermo Fisher Scientific, Waltham, MA USA). Lysates were clarified by centrifugation and the protein concentration was determined using DC protein assay system (Bio-Rad, Hercules, CA USA). Equal amount of protein was resolved by sodium dodecyl sulfate-polyacrylamide gel electrophoresis (SDS-PAGE) using Criterion TGX Stain-Free Precast Gels (Bio-Rad) and transferred onto Immobilon-P membranes (MilliporeSigma, St. Louis, MO USA). Primary antibodies used are listed in the Resource table. Secondary antibodies conjugated

to Horseradish peroxidase were used at a dilution of 1:5-10,000 (Jackson Immunochemicals, West Grove, PA USA). Clarity Western ECL Substrate (Bio-Rad) was then applied to blots and protein levels were detected using autoradiography with ChemiDoc XRS+ Imager (Bio-Rad).

RNA editing site-specific quantitative PCR (RESS-qPCR)

RNA editing fingerprint assay using RESS-qPCR was performed as previously described[88]. Total RNA was isolated from lentivirus-transduced cells using RNeasy Plus Mini Kit including on-column DNase digestion following the manufacturer's protocol. To eliminate any residual genomic DNA contamination, TURBO DNA-free™ Kit (ThermoFisher Scientific) was used to further clean up isolated RNAs. RNAs free of genomic DNA were reverse transcribed to cDNAs using the High-Capacity cDNA Reverse Transcription Kit (Life technologies, CA, USA). Primers used for RESS-qPCR were previously published and are listed in the Resource table[19]. Quantitative RT-PCR was performed using iTaq Universal SYBR Green Supermix (Bio-Rad) on the C1000 Thermal Cycler (Bio-Rad). The relative RNA editing level (Edit/Wild-Type RNA ratio) was calculated as $2^{-(\text{Ct Edit} - \text{Ct WT})}$.

Sanger sequencing to detect RNA editing

Isolated RNAs free of genomic DNA were used for Sanger sequencing analysis to verify RNA editing events. PCR was performed using the high-fidelity Phusion PCR kit according to the manufacturer's instructions (New England Biolabs, Ipswich, MA, E0553). "Outer" primers listed in the Resource table were used to produce amplicons flanking the editing site about 75-125 bp on either side to ensure successful sequencing analysis. Successful PCRs were verified by DNA gel electrophoresis and amplicons were extracted from the gel using Monarch gel extraction kit (BioRad, T1020S) according to manufacturer's instructions and submitted for sequencing

analysis (IDT Technologies). Sanger sequencing was performed using the outer primers (A/G were read for WT/Edited if forward primers were used; T/C were read if reverse primers were used) used for PCR, and sequence chromatograms were analyzed using Chromas software.

Drug screening with ferroptosis-focused library

MDA-MB-231 cells treated with shNT (ADAR1-Intact) or shADAR1 (ADAR1-Deficient) were screened against the ferroptosis-focused drug library (MedChemExpress, Monmouth Junction, NJ, HY-L051) at the High Throughput Screening Center (HTSC) at Washington University in St. Louis. CellTiter-Glo® Luminescent Cell Viability Assay (Promega) was utilized to determine cell viability upon drug treatment as previously described. Cells were prepared in defined medium with low serum using DMEM supplemented with 2% FBS and L-glutamine.

All drugs in the library were pre-dispensed into 96-well sterile polypropylene plates (Corning, Axyen) using a Hummingbird and subsequently diluted with media to produce intermediate plates at 20µM and 2µM. Diluted compounds were then transferred using a BiomekFX (Beckman Coulter) to 96-well white cell culture plates (Greiner Bio-One, Monroe, NC, 655083) (50µl/well, 18 plates total with 9 plates for each experimental group. Select wells containing DMSO alone served as controls. MDA-MB-231 cells treated with shNT (ADAR1-Intact) or shADAR1 (ADAR1-Deficient) were seeded (15,000 cells in 50µl cell culture media per well) using the Multidrop 384 dispenser (Thermo Fisher Scientific, 24291). Plates were kept at room temperature for 30 min before being moved to the incubator (37°C, 5% CO_2) for 24h. On day 2, CellTiter-Glo® Viability Assays were performed using the integrated and automated platform (Beckman Coulter), with library plate-matched shNT and shADAR1 samples alternating between screening steps: Cell plates were equilibrated at room temperature for 30 min in a

Cytomat MPH incubator. CellTiter-Glo® reagent (100µl/well) was added with a Multidrop 384 dispenser. Plates were shaken at 250 rpm for 2 min with a Teleshake followed by room temperature incubation for 1h in a Cytomat MPH incubator. Luminescence was measured (1 sec/well after a 1 min delay) with a Perkin Elmer Envision plate reader. To monitor assay performance, Coefficient of variations (CVs) and Z'-factors for DMSO-treated and no-cell control samples were determined. All screening plates were confirmed to display high quality assay metrics (CVs < 10%; Z'-factors > 0.8). All test wells were normalized to no-treatment samples on the same plate. Relative cell viability was compared between shADAR1 and shNT samples, and the cut-off was set at 51% to discriminate hits from no-hits.

Mammary fat pad orthotopic implantation

Immuno-deficient NOD scid gamma (NSG) female mice at 6-8 weeks old were purchased from Jackson Laboratory (Bar Harbor, ME, USA, 005557) and placed on Teklad Global 18% protein rodent diet (Envigo, Indianapolis, USA, T.2918.15) 3 days before implantation. 1.5 x 10^5 MDA-MB-231 cells were harvested and resuspended in PBS, mixed with Matrigel® Matrix Basement Membrane (Corning, Waltham, USA, 354230) at 1:1 volume ratio, and kept at 4°C until implantation. In total 100µl of cells-Matrigel solutions were injected into the right inguinal mammary glands of NSG mice. Ten days after the implantation, palpable tumors were detected and half of the mice were switched to doxycycline-containing diet (Envigo, 625mg/kg, TD.01306). Tumors were measured using a caliper once per week, and tumor volumes were calculated using the following formula: $L \times W^2 \times 0.52$ (L and W represents the large and small diameter of the tumor, respectively). Mice were euthanized 6 weeks post implantation or before tumors reached 2 cubic cm in size. Tumors were dissected from the mice for weight measurement and subsequently fixed in 10% formalin, before transferred to 70% ethanol for

processing to prepare formalin-fixed paraffin-embedded (FFPE) tissue blocks. All animal-related experimental procedures were performed in compliance with the guidelines given by the American Association for Accreditation for Laboratory Animal Care and the U.S. Public Health Service Policy on Human Care and Use of Laboratory Animals. All animal studies were approved by the Washington University Institutional Animal Care and Use Committee (IACUC) in accordance with the Animal Welfare Act and NIH guidelines (Protocol 20220144).

Immunohistochemistry

Tumor FFPE tissue blocks were sectioned at 5μm thickness. Hematoxylin and eosin (H&E) staining was performed for histological evaluations. For immunohistochemistry, sections were stained using a Bond RXm autostainer (Leica, Buffalo Grove, IL USA). Primary antibodies for ADAR1-p150 (Abcam, ab126745) and 4-Hydroxynonenal (4HNE, ThermoFisher Scientific, MA5-27570) were diluted 1:100 in Antibody Diluent (Leica). Briefly, slides were baked at 65°C for 15min and automated software performed dewaxing, rehydration, antigen retrieval, blocking, primary antibody incubation, post primary antibody incubation, detection (DAB), and counterstaining using Bond reagents (Leica). Samples were then removed from the machine, dehydrated through ethanols and xylenes, mounted and cover slipped before imaging.

Bioinformatic analysis and data availability

Bioinformatic analyses to assess relationships among gene expression, drug response, gene dependency and metabolomics in breast cancer cell lines were performed using the DepMap public data (depmap.org) with the TNBC (HCC1187, HS578T, HCC1599, DU4475, BT549, HCC1143, BT20, MDA-MB-436, HCC1806, HCC70, HCC2157, HCC1395, MDA-MB-231, MDA-MB-468, MDA-MB-453) and non-TNBC (SKBR3, MCF7, KPL1, MDA-MB-134VI,

ZR751, EFM192A, T47D, AU565, HCC1419, EFM19, HCC1500, HCC1428, UACC893, UACC812, HCC202, HCC2218, MDA-MB-175VII, BT483, ZR7530, MDA-MB-415, BT474, HCC1569, MDA-MB-361) groups[89]. The results published here are in whole or part based upon data generated by Cancer Target Discovery and Development (CTD²) Network (https://ccg.cancer.gov/ccg/research/functional-genomics/ctd2/data-portal) established by the National Cancer Institute's Center for Cancer Genomics. RNA-seq data from this study are available at the Gene Expression Omnibus under accession number GSE286185.

Statistical analysis

All *in vitro* and *in vivo* data are reported as the mean ± SD unless stated otherwise, and statistical analyses were performed using GraphPad Prism 10. The two-tailed unpaired student t test was performed for experiments comparing between two experimental groups. One-way ANOVA with Tukey's multiple comparisons was used for statistical analysis of all other experiments unless stated otherwise. Tumor volume analyses from *in vivo* studies were performed by 1) comparing AUC (area under curve) between experimental groups using one-way ANOVA, and 2) comparing weekly measured tumor volumes between groups using two-way ANOVA with Tukey's multiple comparison. Pearson correlation coefficient and/or Spearman's rank correlation coefficient were calculated to assess correlations between two data sets. Statistical significance was evaluated using p-value, which is shown in the numerical format. Lower p-values reject the null hypothesis more strongly, and p-value <0.05 is generally considered statistically significant.

Acknowledgements

We thank the Division of Comparative Medicine at Washington University in St. Louis for housing the mouse colony. We thank the Denardo lab for processing the fixed tumor tissues. We

thank the Tissue Histology Core, Department of Obstetrics and Gynecology, for sectioning the tumor samples and performing H&E staining. We thank the support by the Genome Technology Access Center (GTAC) at McDonnell Genome Institute (MGI) Symposium Pilot Project Funding to perform RNA-seq analyses (Catrina Fronick and Michael Heinz for logistics; Toni Sinnwell, Elliott Klotz, and Eric Tycksen for quality control, sequencing and analyses). We acknowledge the Just-In-Time (JIT) Core Usage Funding Program to support the collaboration with HTSC for drug screening. Both GTAC@MGI Symposium Pilot Project and JIT programs are funded through the Institute of Clinical and Translational Sciences (ICTS), Washington University in St. Louis. ICTS was supported by the National Center for Advancing Translational Sciences (NCATS) grant UL1TR002345. This work was supported by R01CA262804 (JDW) from the National Cancer Institute, and W81XWH-21-1-0476 and W81XWH-21-1-0466 from the Congressionally Directed Medical Research Programs (CDMRP), Department of Defense (JDW). L.S.T. is supported by R25HG006687 and T32GM148405 from National Human Genome Research Institute and National Institute of General Medical Sciences, respectively.

Author Contributions

C-P. Kung: Conceptualization, investigation, methodology, formal analysis, project administration, writing–original draft, writing–review and editing. **N.D. Terzich:** investigation, methodology, formal analysis. **MXG. Ilagen:** investigation, methodology, formal analysis, writing–review and editing. **M.J. Prinsen:** Investigation, methodology, formal analysis. **M. Kaushal:** Investigation, methodology, formal analysis. **R.D. Kladney:** Investigation, methodology. **J.H. Weber:** Investigation. **A.R. Mabry:** Investigation. **L.S. Torres:** Investigation. **E.R. Bramel:** Investigation. **E.C. Freeman:** Investigation. **T. Sabloak:** Investigation. **K.A. Cottrell:** Investigation. **S. Ryu:** Investigation. **W.M. Weber:** Investigation.

L. Maggi Jr.: investigation, writing–review and editing. **L.P. Shriver:** investigation, methodology, writing–review and editing. **G.J. Patti:** funding acquisition, investigation, writing–review and editing. **J.D. Weber:** Conceptualization, resources, supervision, funding acquisition, writing–original draft, writing–review and editing.

Declaration of Interests

G.J. Patti is the Chief Scientific Officer of Panome Bio, a scientific advisory board member for Cambridge Isotope Laboratories, and has a collaborative research agreement with Agilent Technologies.

References

1. Ademuyiwa, F.O., Tao, Y., Luo, J., Weilbaecher, K., and Ma, C.X. (2017). Differences in the mutational landscape of triple-negative breast cancer in African Americans and Caucasians. Breast Cancer Res Treat *161*, 491-499. 10.1007/s10549-016-4062-y.
2. Obidiro, O., Battogtokh, G., and Akala, E.O. (2023). Triple Negative Breast Cancer Treatment Options and Limitations: Future Outlook. Pharmaceutics *15*. 10.3390/pharmaceutics15071796.
3. Loizides, S., and Constantinidou, A. (2022). Triple negative breast cancer: Immunogenicity, tumor microenvironment, and immunotherapy. Front Genet *13*, 1095839. 10.3389/fgene.2022.1095839.
4. Zhou, L., and Yu, C.W. (2024). Epigenetic modulations in triple-negative breast cancer: Therapeutic implications for tumor microenvironment. Pharmacol Res *204*, 107205. 10.1016/j.phrs.2024.107205.
5. Munkacsy, G., Santarpia, L., and Gyorffy, B. (2023). Therapeutic Potential of Tumor Metabolic Reprogramming in Triple-Negative Breast Cancer. Int J Mol Sci *24*. 10.3390/ijms24086945.
6. Stockwell, B.R. (2022). Ferroptosis turns 10: Emerging mechanisms, physiological functions, and therapeutic applications. Cell *185*, 2401-2421. 10.1016/j.cell.2022.06.003.
7. Timmerman, L.A., Holton, T., Yuneva, M., Louie, R.J., Padro, M., Daemen, A., Hu, M., Chan, D.A., Ethier, S.P., van 't Veer, L.J., et al. (2013). Glutamine sensitivity analysis identifies the xCT antiporter as a common triple-negative breast tumor therapeutic target. Cancer Cell *24*, 450-465. 10.1016/j.ccr.2013.08.020.
8. Beatty, A., Fink, L.S., Singh, T., Strigun, A., Peter, E., Ferrer, C.M., Nicolas, E., Cai, K.Q., Moran, T.P., Reginato, M.J., et al. (2018). Metabolite Profiling Reveals the Glutathione Biosynthetic Pathway as a Therapeutic Target in Triple-Negative Breast Cancer. Mol Cancer Ther *17*, 264-275. 10.1158/1535-7163.MCT-17-0407.
9. Verma, N., Vinik, Y., Saroha, A., Nair, N.U., Ruppin, E., Mills, G., Karn, T., Dubey, V., Khera, L., Raj, H., et al. (2020). Synthetic lethal combination targeting BET uncovered intrinsic susceptibility of TNBC to ferroptosis. Sci Adv *6*. 10.1126/sciadv.aba8968.
10. Pinnix, Z.K., Miller, L.D., Wang, W., D'Agostino, R., Jr., Kute, T., Willingham, M.C., Hatcher, H., Tesfay, L., Sui, G., Di, X., et al. (2010). Ferroportin and iron regulation in breast cancer progression and prognosis. Sci Transl Med *2*, 43ra56. 10.1126/scitranslmed.3001127.
11. Doll, S., Proneth, B., Tyurina, Y.Y., Panzilius, E., Kobayashi, S., Ingold, I., Irmler, M., Beckers, J., Aichler, M., Walch, A., et al. (2017). ACSL4 dictates ferroptosis sensitivity by shaping cellular lipid composition. Nat Chem Biol *13*, 91-98. 10.1038/nchembio.2239.
12. Beatty, A., Singh, T., Tyurina, Y.Y., Tyurin, V.A., Samovich, S., Nicolas, E., Maslar, K., Zhou, Y., Cai, K.Q., Tan, Y., et al. (2021). Ferroptotic cell death triggered by conjugated linolenic acids is mediated by ACSL1. Nat Commun *12*, 2244. 10.1038/s41467-021-22471-y.
13. Lorito, N., Subbiani, A., Smiriglia, A., Bacci, M., Bonechi, F., Tronci, L., Romano, E., Corrado, A., Longo, D.L., Iozzo, M., et al. (2024). FADS1/2 control lipid metabolism and ferroptosis susceptibility in triple-negative breast cancer. EMBO Mol Med *16*, 1533-1559. 10.1038/s44321-024-00090-6.
14. Fumagalli, D., Gacquer, D., Rothe, F., Lefort, A., Libert, F., Brown, D., Kheddoumi, N., Shlien, A., Konopka, T., Salgado, R., et al. (2015). Principles Governing A-to-I RNA

Editing in the Breast Cancer Transcriptome. Cell Rep *13*, 277-289. 10.1016/j.celrep.2015.09.032.

15. Peng, X., Xu, X., Wang, Y., Hawke, D.H., Yu, S., Han, L., Zhou, Z., Mojumdar, K., Jeong, K.J., Labrie, M., et al. (2018). A-to-I RNA Editing Contributes to Proteomic Diversity in Cancer. Cancer Cell *33*, 817-828 e817. 10.1016/j.ccell.2018.03.026.
16. Han, L., Diao, L., Yu, S., Xu, X., Li, J., Zhang, R., Yang, Y., Werner, H.M.J., Eterovic, A.K., Yuan, Y., et al. (2015). The Genomic Landscape and Clinical Relevance of A-to-I RNA Editing in Human Cancers. Cancer Cell *28*, 515-528. 10.1016/j.ccell.2015.08.013.
17. Paz-Yaacov, N., Bazak, L., Buchumenski, I., Porath, H.T., Danan-Gotthold, M., Knisbacher, B.A., Eisenberg, E., and Levanon, E.Y. (2015). Elevated RNA Editing Activity Is a Major Contributor to Transcriptomic Diversity in Tumors. Cell Rep *13*, 267-276. 10.1016/j.celrep.2015.08.080.
18. Baker, A.R., Miliotis, C., Ramirez-Moya, J., Marc, T., Vlachos, I.S., Santisteban, P., and Slack, F.J. (2022). Transcriptome Profiling of ADAR1 Targets in Triple-Negative Breast Cancer Cells Reveals Mechanisms for Regulating Growth and Invasion. Mol Cancer Res *20*, 960-971. 10.1158/1541-7786.MCR-21-0604.
19. Kung, C.P., Cottrell, K.A., Ryu, S., Bramel, E.R., Kladney, R.D., Bao, E.A., Freeman, E.C., Sabloak, T., Maggi, L., Jr., and Weber, J.D. (2021). Evaluating the therapeutic potential of ADAR1 inhibition for triple-negative breast cancer. Oncogene *40*, 189-202. 10.1038/s41388-020-01515-5.
20. Ishizuka, J.J., Manguso, R.T., Cheruiyot, C.K., Bi, K., Panda, A., Iracheta-Vellve, A., Miller, B.C., Du, P.P., Yates, K.B., Dubrot, J., et al. (2019). Loss of ADAR1 in tumours overcomes resistance to immune checkpoint blockade. Nature *565*, 43-48. 10.1038/s41586-018-0768-9.
21. Gannon, H.S., Zou, T., Kiessling, M.K., Gao, G.F., Cai, D., Choi, P.S., Ivan, A.P., Buchumenski, I., Berger, A.C., Goldstein, J.T., et al. (2018). Identification of ADAR1 adenosine deaminase dependency in a subset of cancer cells. Nat Commun *9*, 5450. 10.1038/s41467-018-07824-4.
22. Liu, H., Golji, J., Brodeur, L.K., Chung, F.S., Chen, J.T., deBeaumont, R.S., Bullock, C.P., Jones, M.D., Kerr, G., Li, L., et al. (2019). Tumor-derived IFN triggers chronic pathway agonism and sensitivity to ADAR loss. Nat Med *25*, 95-102. 10.1038/s41591-018-0302-5.
23. Karki, R., Sundaram, B., Sharma, B.R., Lee, S., Malireddi, R.K.S., Nguyen, L.N., Christgen, S., Zheng, M., Wang, Y., Samir, P., et al. (2021). ADAR1 restricts ZBP1-mediated immune response and PANoptosis to promote tumorigenesis. Cell Rep *37*, 109858. 10.1016/j.celrep.2021.109858.
24. Zhang, T., Yin, C., Fedorov, A., Qiao, L., Bao, H., Beknazarov, N., Wang, S., Gautam, A., Williams, R.M., Crawford, J.C., et al. (2022). ADAR1 masks the cancer immunotherapeutic promise of ZBP1-driven necroptosis. Nature *606*, 594-602. 10.1038/s41586-022-04753-7.
25. Mehdipour, P., Marhon, S.A., Ettayebi, I., Chakravarthy, A., Hosseini, A., Wang, Y., de Castro, F.A., Loo Yau, H., Ishak, C., Abelson, S., et al. (2020). Epigenetic therapy induces transcription of inverted SINEs and ADAR1 dependency. Nature *588*, 169-173. 10.1038/s41586-020-2844-1.
26. McGuirk, S., Audet-Delage, Y., and St-Pierre, J. (2020). Metabolic Fitness and Plasticity in Cancer Progression. Trends Cancer *6*, 49-61. 10.1016/j.trecan.2019.11.009.

27. Kung, C.P., Maggi, L.B., Jr., and Weber, J.D. (2018). The Role of RNA Editing in Cancer Development and Metabolic Disorders. Front Endocrinol (Lausanne) *9*, 762. 10.3389/fendo.2018.00762.
28. Yang, C.C., Chen, Y.T., Chang, Y.F., Liu, H., Kuo, Y.P., Shih, C.T., Liao, W.C., Chen, H.W., Tsai, W.S., and Tan, B.C. (2017). ADAR1-mediated 3' UTR editing and expression control of antiapoptosis genes fine-tunes cellular apoptosis response. Cell Death Dis *8*, e2833. 10.1038/cddis.2017.12.
29. Venkatesh, D., O'Brien, N.A., Zandkarimi, F., Tong, D.R., Stokes, M.E., Dunn, D.E., Kengmana, E.S., Aron, A.T., Klein, A.M., Csuka, J.M., et al. (2020). MDM2 and MDMX promote ferroptosis by PPARalpha-mediated lipid remodeling. Genes Dev *34*, 526-543. 10.1101/gad.334219.119.
30. Liu, J., Kang, R., and Tang, D. (2024). Adverse effects of ferroptotic therapy: mechanisms and management. Trends Cancer *10*, 417-429. 10.1016/j.trecan.2024.01.002.
31. Zhao, L., Zhou, X., Xie, F., Zhang, L., Yan, H., Huang, J., Zhang, C., Zhou, F., Chen, J., and Zhang, L. (2022). Ferroptosis in cancer and cancer immunotherapy. Cancer Commun (Lond) *42*, 88-116. 10.1002/cac2.12250.
32. Ma, S., Henson, E.S., Chen, Y., and Gibson, S.B. (2016). Ferroptosis is induced following siramesine and lapatinib treatment of breast cancer cells. Cell Death Dis *7*, e2307. 10.1038/cddis.2016.208.
33. Ostenfeld, M.S., Fehrenbacher, N., Hoyer-Hansen, M., Thomsen, C., Farkas, T., and Jaattela, M. (2005). Effective tumor cell death by sigma-2 receptor ligand siramesine involves lysosomal leakage and oxidative stress. Cancer Res *65*, 8975-8983. 10.1158/0008-5472.CAN-05-0269.
34. Gagliardi, M., Cotella, D., Santoro, C., Cora, D., Barlev, N.A., Piacentini, M., and Corazzari, M. (2019). Aldo-keto reductases protect metastatic melanoma from ER stress-independent ferroptosis. Cell Death Dis *10*, 902. 10.1038/s41419-019-2143-7.
35. Haq, R., Shoag, J., Andreu-Perez, P., Yokoyama, S., Edelman, H., Rowe, G.C., Frederick, D.T., Hurley, A.D., Nellore, A., Kung, A.L., et al. (2013). Oncogenic BRAF regulates oxidative metabolism via PGC1alpha and MITF. Cancer Cell *23*, 302-315. 10.1016/j.ccr.2013.02.003.
36. Gao, F., Zhang, B., Sun, Z., Gao, Y., Liu, C., Dou, X., Tong, H., and Wang, R. (2023). Regulation of endothelial ferroptosis by SESN1 in atherosclerosis and its related mechanism. Aging (Albany NY) *15*, 5052-5065. 10.18632/aging.204777.
37. Dixon, S.J., Patel, D.N., Welsch, M., Skouta, R., Lee, E.D., Hayano, M., Thomas, A.G., Gleason, C.E., Tatonetti, N.P., Slusher, B.S., and Stockwell, B.R. (2014). Pharmacological inhibition of cystine-glutamate exchange induces endoplasmic reticulum stress and ferroptosis. Elife *3*, e02523. 10.7554/eLife.02523.
38. Lee, C.H., Ying, T.H., Chiou, H.L., Hsieh, S.C., Wen, S.H., Chou, R.H., and Hsieh, Y.H. (2017). Alpha-mangostin induces apoptosis through activation of reactive oxygen species and ASK1/p38 signaling pathway in cervical cancer cells. Oncotarget *8*, 47425-47439. 10.18632/oncotarget.17659.
39. Shi, Y., Fan, Y., Hu, Y., Jing, J., Wang, C., Wu, Y., Geng, Q., Dong, X., Li, E., and Dong, D. (2020). alpha-Mangostin suppresses the de novo lipogenesis and enhances the chemotherapeutic response to gemcitabine in gallbladder carcinoma cells via targeting the AMPK/SREBP1 cascades. J Cell Mol Med *24*, 760-771. 10.1111/jcmm.14785.

40. Gilbert, N.C., Gerstmeier, J., Schexnaydre, E.E., Borner, F., Garscha, U., Neau, D.B., Werz, O., and Newcomer, M.E. (2020). Structural and mechanistic insights into 5-lipoxygenase inhibition by natural products. Nat Chem Biol *16*, 783-790. 10.1038/s41589-020-0544-7.
41. Sun, Q.Y., Zhou, H.H., and Mao, X.Y. (2019). Emerging Roles of 5-Lipoxygenase Phosphorylation in Inflammation and Cell Death. Oxid Med Cell Longev *2019*, 2749173. 10.1155/2019/2749173.
42. Bhatt, V., Lan, T., Wang, W., Kong, J., Lopes, E.C., Wang, J., Khayati, K., Raju, A., Rangel, M., Lopez, E., et al. (2023). Inhibition of autophagy and MEK promotes ferroptosis in Lkb1-deficient Kras-driven lung tumors. Cell Death Dis *14*, 61. 10.1038/s41419-023-05592-8.
43. Yin, J., Chen, J., Hong, J.H., Huang, Y., Xiao, R., Liu, S., Deng, P., Sun, Y., Chai, K.X.Y., Zeng, X., et al. (2024). 4EBP1-mediated SLC7A11 protein synthesis restrains ferroptosis triggered by MEK inhibitors in advanced ovarian cancer. JCI Insight *9*. 10.1172/jci.insight.177857.
44. Larkin, J., Ascierto, P.A., Dreno, B., Atkinson, V., Liszkay, G., Maio, M., Mandala, M., Demidov, L., Stroyakovskiy, D., Thomas, L., et al. (2014). Combined vemurafenib and cobimetinib in BRAF-mutated melanoma. N Engl J Med *371*, 1867-1876. 10.1056/NEJMoa1408868.
45. Diamond, E.L., Durham, B.H., Ulaner, G.A., Drill, E., Buthorn, J., Ki, M., Bitner, L., Cho, H., Young, R.J., Francis, J.H., et al. (2019). Efficacy of MEK inhibition in patients with histiocytic neoplasms. Nature *567*, 521-524. 10.1038/s41586-019-1012-y.
46. Brufsky, A., Kim, S.B., Zvirbule, Z., Eniu, A., Mebis, J., Sohn, J.H., Wongchenko, M., Chohan, S., Amin, R., Yan, Y., et al. (2021). A phase II randomized trial of cobimetinib plus chemotherapy, with or without atezolizumab, as first-line treatment for patients with locally advanced or metastatic triple-negative breast cancer (COLET): primary analysis. Ann Oncol *32*, 652-660. 10.1016/j.annonc.2021.01.065.
47. Han, H.S., Vikas, P., Costa, R.L.B., Jahan, N., Taye, A., and Stringer-Reasor, E.M. (2023). Early-Stage Triple-Negative Breast Cancer Journey: Beginning, End, and Everything in Between. Am Soc Clin Oncol Educ Book *43*, e390464. 10.1200/EDBK_390464.
48. Yin, C., Zhang, M.M., Wang, G.L., Deng, X.Y., Tu, Z., Jiang, S.S., Gao, Z.D., Hao, M., Chen, Y., Li, Y., and Yang, S.Y. (2024). Loss of ADAR1 induces ferroptosis of breast cancer cells. Cell Signal *121*, 111258. 10.1016/j.cellsig.2024.111258.
49. He, D., Niu, C., Bai, R., Chen, N., and Cui, J. (2024). ADAR1 Promotes Invasion and Migration and Inhibits Ferroptosis via the FAK/AKT Pathway in Colorectal Cancer. Mol Carcinog. 10.1002/mc.23818.
50. Murray, M.B., Leak, L.B., Lee, W.C., and Dixon, S.J. (2023). Protocol for detection of ferroptosis in cultured cells. STAR Protoc *4*, 102457. 10.1016/j.xpro.2023.102457.
51. Leu, J.I., Murphy, M.E., and George, D.L. (2019). Mechanistic basis for impaired ferroptosis in cells expressing the African-centric S47 variant of p53. Proc Natl Acad Sci U S A *116*, 8390-8396. 10.1073/pnas.1821277116.
52. Enache, O.M., Rendo, V., Abdusamad, M., Lam, D., Davison, D., Pal, S., Currimjee, N., Hess, J., Pantel, S., Nag, A., et al. (2020). Cas9 activates the p53 pathway and selects for p53-inactivating mutations. Nat Genet *52*, 662-668. 10.1038/s41588-020-0623-4.

53. Gnanapradeepan, K., Basu, S., Barnoud, T., Budina-Kolomets, A., Kung, C.P., and Murphy, M.E. (2018). The p53 Tumor Suppressor in the Control of Metabolism and Ferroptosis. Front Endocrinol (Lausanne) *9*, 124. 10.3389/fendo.2018.00124.
54. Pagliarini, R., Shao, W., and Sellers, W.R. (2015). Oncogene addiction: pathways of therapeutic response, resistance, and road maps toward a cure. EMBO Rep *16*, 280-296. 10.15252/embr.201439949.
55. Nagel, R., Semenova, E.A., and Berns, A. (2016). Drugging the addict: non-oncogene addiction as a target for cancer therapy. EMBO Rep *17*, 1516-1531. 10.15252/embr.201643030.
56. Mendez Ruiz, S., Chalk, A.M., Goradia, A., Heraud-Farlow, J., and Walkley, C.R. (2023). Over-expression of ADAR1 in mice does not initiate or accelerate cancer formation in vivo. NAR Cancer *5*, zcad023. 10.1093/narcan/zcad023.
57. Xie, Y., Wang, B., Zhao, Y., Tao, Z., Wang, Y., Chen, G., and Hu, X. (2022). Mammary adipocytes protect triple-negative breast cancer cells from ferroptosis. J Hematol Oncol *15*, 72. 10.1186/s13045-022-01297-1.
58. Ackermann, T., Shokry, E., Deshmukh, R., Anand, J., Galbraith, L.C.A., Mitchell, L., Rodriguez-Blanco, G., Villar, V.H., Sterken, B.A., Nixon, C., et al. (2024). Breast cancer secretes anti-ferroptotic MUFAs and depends on selenoprotein synthesis for metastasis. EMBO Mol Med *16*, 2749-2774. 10.1038/s44321-024-00142-x.
59. Puente-Cobacho, B., Esteo, C., Altea-Manzano, P., Garcia-Perez, J.L., Quiles, J.L., Sanchez-Rovira, P., Martín-Salvago, M.D., Molina-Jiménez, L., Luque, R.J., Fendt, S.-M., and Vera-Ramirez, L. (2024). De novo lipogenesis protects dormant breast cancer cells from ferroptosis and promotes metastasis. Redox Biology, 103480. https://doi.org/10.1016/j.redox.2024.103480.
60. Park, S.Y., Jeong, K.J., Poire, A., Zhang, D., Tsang, Y.H., Blucher, A.S., and Mills, G.B. (2023). Irreversible HER2 inhibitors overcome resistance to the RSL3 ferroptosis inducer in non-HER2 amplified luminal breast cancer. Cell Death Dis *14*, 532. 10.1038/s41419-023-06042-1.
61. Bajbouj, K., Shafarin, J., and Hamad, M. (2019). Estrogen-dependent disruption of intracellular iron metabolism augments the cytotoxic effects of doxorubicin in select breast and ovarian cancer cells. Cancer Manag Res *11*, 4655-4668. 10.2147/CMAR.S204852.
62. Li, X., Rhee, D.K., Malhotra, R., Mayeur, C., Hurst, L.A., Ager, E., Shelton, G., Kramer, Y., McCulloh, D., Keefe, D., et al. (2016). Progesterone receptor membrane component-1 regulates hepcidin biosynthesis. J Clin Invest *126*, 389-401. 10.1172/JCI83831.
63. Liu, L., Zhang, C., Qu, S., Liu, R., Chen, H., Liang, Z., Tian, Z., Li, L., Ma, S., and Liu, X. (2022). ESR1 inhibits ionizing radiation-induced ferroptosis in breast cancer cells via the NEDD4L/CD71 pathway. Arch Biochem Biophys *725*, 109299. 10.1016/j.abb.2022.109299.
64. Wang, H., Hou, M.J., Liao, L., Li, P., Chen, T., Wang, P., and Zhu, B.T. (2024). Strong Protection by 4-Hydroxyestrone against Erastin-Induced Ferroptotic Cell Death in Estrogen Receptor-Negative Human Breast Cancer Cells: Evidence for Protein Disulfide Isomerase as a Mechanistic Target for Protection. Biochemistry *63*, 984-999. 10.1021/acs.biochem.3c00261.
65. Cancer Genome Atlas, N. (2012). Comprehensive molecular portraits of human breast tumours. Nature *490*, 61-70. 10.1038/nature11412.

66. Dibra, D., Xiong, S., Moyer, S.M., El-Naggar, A.K., Qi, Y., Su, X., Kong, E.K., Korkut, A., and Lozano, G. (2024). Mutant p53 protects triple-negative breast adenocarcinomas from ferroptosis in vivo. Sci Adv *10*, eadk1835. 10.1126/sciadv.adk1835.
67. Adams, C.M., Mitra, R., Xiao, Y., Michener, P., Palazzo, J., Chao, A., Gour, J., Cassel, J., Salvino, J.M., and Eischen, C.M. (2023). Targeted MDM2 Degradation Reveals a New Vulnerability for p53-Inactivated Triple-Negative Breast Cancer. Cancer Discov *13*, 1210-1229. 10.1158/2159-8290.CD-22-1131.
68. Kung, C.P., and Weber, J.D. (2022). It's Getting Complicated-A Fresh Look at p53-MDM2-ARF Triangle in Tumorigenesis and Cancer Therapy. Front Cell Dev Biol *10*, 818744. 10.3389/fcell.2022.818744.
69. Cottrell, K.A., Torres, L.S., Dizon, M.G., and Weber, J.D. (2021). 8-azaadenosine and 8-chloroadenosine are not selective inhibitors of ADAR. Cancer Res Commun *1*, 56-64. 10.1158/2767-9764.crc-21-0027.
70. Weth, F.R., Hoggarth, G.B., Weth, A.F., Paterson, E., White, M.P.J., Tan, S.T., Peng, L., and Gray, C. (2024). Unlocking hidden potential: advancements, approaches, and obstacles in repurposing drugs for cancer therapy. Br J Cancer *130*, 703-715. 10.1038/s41416-023-02502-9.
71. Rehwinkel, J., and Mehdipour, P. (2024). ADAR1: from basic mechanisms to inhibitors. Trends Cell Biol. 10.1016/j.tcb.2024.06.006.
72. Lee, J., Lim, B., Pearson, T., Choi, K., Fuson, J.A., Bartholomeusz, C., Paradiso, L.J., Myers, T., Tripathy, D., and Ueno, N.T. (2019). Anti-tumor and anti-metastasis efficacy of E6201, a MEK1 inhibitor, in preclinical models of triple-negative breast cancer. Breast Cancer Res Treat *175*, 339-351. 10.1007/s10549-019-05166-3.
73. Lulli, D., Carbone, M.L., and Pastore, S. (2017). The MEK Inhibitors Trametinib and Cobimetinib Induce a Type I Interferon Response in Human Keratinocytes. Int J Mol Sci *18*. 10.3390/ijms18102227.
74. Jennis, M., Kung, C.P., Basu, S., Budina-Kolomets, A., Leu, J.I., Khaku, S., Scott, J.P., Cai, K.Q., Campbell, M.R., Porter, D.K., et al. (2016). An African-specific polymorphism in the TP53 gene impairs p53 tumor suppressor function in a mouse model. Genes Dev *30*, 918-930. 10.1101/gad.275891.115.
75. Yang, F., Xiao, Y., Ding, J.H., Jin, X., Ma, D., Li, D.Q., Shi, J.X., Huang, W., Wang, Y.P., Jiang, Y.Z., and Shao, Z.M. (2023). Ferroptosis heterogeneity in triple-negative breast cancer reveals an innovative immunotherapy combination strategy. Cell Metab *35*, 84-100 e108. 10.1016/j.cmet.2022.09.021.
76. Bhate, A., Sun, T., and Li, J.B. (2019). ADAR1: A New Target for Immuno-oncology Therapy. Mol Cell *73*, 866-868. 10.1016/j.molcel.2019.02.021.
77. Deng, J., Zhou, M., Liao, T., Kuang, W., Xia, H., Yin, Z., Tan, Q., Li, Y., Song, S., Zhou, E., and Jin, Y. (2022). Targeting Cancer Cell Ferroptosis to Reverse Immune Checkpoint Inhibitor Therapy Resistance. Front Cell Dev Biol *10*, 818453. 10.3389/fcell.2022.818453.
78. Ferrer, M., Mourikis, N., Davidson, E.E., Kleeman, S.O., Zaccaria, M., Habel, J., Rubino, R., Gao, Q., Flint, T.R., Young, L., et al. (2023). Ketogenic diet promotes tumor ferroptosis but induces relative corticosterone deficiency that accelerates cachexia. Cell Metab *35*, 1147-1162 e1147. 10.1016/j.cmet.2023.05.008.
79. Salvadori, G., Zanardi, F., Iannelli, F., Lobefaro, R., Vernieri, C., and Longo, V.D. (2021). Fasting-mimicking diet blocks triple-negative breast cancer and cancer stem cell escape. Cell Metab *33*, 2247-2259 e2246. 10.1016/j.cmet.2021.10.008.

80. Martinez-Garay, C., and Djouder, N. (2023). Dietary interventions and precision nutrition in cancer therapy. Trends Mol Med *29*, 489-511. 10.1016/j.molmed.2023.04.004.
81. Koelmel, J.P., Li, X., Stow, S.M., Sartain, M.J., Murali, A., Kemperman, R., Tsugawa, H., Takahashi, M., Vasiliou, V., Bowden, J.A., et al. (2020). Lipid Annotator: Towards Accurate Annotation in Non-Targeted Liquid Chromatography High-Resolution Tandem Mass Spectrometry (LC-HRMS/MS) Lipidomics Using A Rapid and User-Friendly Software. Metabolites *10*. 10.3390/metabo10030101.
82. Subramanian, A., Tamayo, P., Mootha, V.K., Mukherjee, S., Ebert, B.L., Gillette, M.A., Paulovich, A., Pomeroy, S.L., Golub, T.R., Lander, E.S., and Mesirov, J.P. (2005). Gene set enrichment analysis: a knowledge-based approach for interpreting genome-wide expression profiles. Proc Natl Acad Sci U S A *102*, 15545-15550. 10.1073/pnas.0506580102.
83. Ashburner, M., Ball, C.A., Blake, J.A., Botstein, D., Butler, H., Cherry, J.M., Davis, A.P., Dolinski, K., Dwight, S.S., Eppig, J.T., et al. (2000). Gene ontology: tool for the unification of biology. The Gene Ontology Consortium. Nat Genet *25*, 25-29. 10.1038/75556.
84. Gene Ontology, C., Aleksander, S.A., Balhoff, J., Carbon, S., Cherry, J.M., Drabkin, H.J., Ebert, D., Feuermann, M., Gaudet, P., Harris, N.L., et al. (2023). The Gene Ontology knowledgebase in 2023. Genetics *224*. 10.1093/genetics/iyad031.
85. Xie, Z., Bailey, A., Kuleshov, M.V., Clarke, D.J.B., Evangelista, J.E., Jenkins, S.L., Lachmann, A., Wojciechowicz, M.L., Kropiwnicki, E., Jagodnik, K.M., et al. (2021). Gene Set Knowledge Discovery with Enrichr. Curr Protoc *1*, e90. 10.1002/cpz1.90.
86. Chen, E.Y., Tan, C.M., Kou, Y., Duan, Q., Wang, Z., Meirelles, G.V., Clark, N.R., and Ma'ayan, A. (2013). Enrichr: interactive and collaborative HTML5 gene list enrichment analysis tool. BMC Bioinformatics *14*, 128. 10.1186/1471-2105-14-128.
87. Mootha, V.K., Lindgren, C.M., Eriksson, K.F., Subramanian, A., Sihag, S., Lehar, J., Puigserver, P., Carlsson, E., Ridderstrale, M., Laurila, E., et al. (2003). PGC-1alpha-responsive genes involved in oxidative phosphorylation are coordinately downregulated in human diabetes. Nat Genet *34*, 267-273. 10.1038/ng1180.
88. Crews, L.A., Jiang, Q., Zipeto, M.A., Lazzari, E., Court, A.C., Ali, S., Barrett, C.L., Frazer, K.A., and Jamieson, C.H. (2015). An RNA editing fingerprint of cancer stem cell reprogramming. J Transl Med *13*, 52. 10.1186/s12967-014-0370-3.
89. Tsherniak, A., Vazquez, F., Montgomery, P.G., Weir, B.A., Kryukov, G., Cowley, G.S., Gill, S., Harrington, W.F., Pantel, S., Krill-Burger, J.M., et al. (2017). Defining a Cancer Dependency Map. Cell *170*, 564-576 e516. 10.1016/j.cell.2017.06.010.

Figure 1. ADAR1 protects TNBC cells from ferroptosis induction

A) Light micrographs of ADAR1-Intact (shNT) and ADAR1-Deficient (shADAR1) MDA-MB-231 TNBC cells treated with different concentrations of RSL3 for 24h. Cell viability analyses were performed to determine IC_{50} values of ferroptosis inducers **B)** RSL3 and **C)** ML162 for ADAR1-Intact and ADAR1-Deficient MDA-MB-231 cells. IC_{50} values of RSL3 were then determined for ADAR1-Intact and ADAR1-Deficient **D)** MDA-MB-436, **E)** HCC1806, and **F)** MDA-MB-468 TNBC cells. Cell viability graphs are representatives of three independent experiments. FC, fold-change. **G)** Immunoblot analysis showed similar levels of ADAR1 knockdown in doxycycline-treated MDA-MB-231 cells possessing Tet-inducible shADAR1 compared to MDA-MB-231 cells treated with shADAR1-containing lentivirus. Images are representative of three replicates. GAPDH, loading control. **H)** MDA-MB-231 cells (1.5×10^5 per mouse) possessing Tet-inducible shADAR1 were injected into mammary fat pads of female NSG mice through orthotopic implantations. Ten days post implantation, half of the mice were switched to doxycycline-containing (625mg/kg) diet. Two days after the diet switch, both control- and doxycycline-diet mice were subjected to RSL3 treatments through i.p. injection (100mg/kg weight; twice a week) for 5 weeks before tumors were resected. **I)** Progression of overall tumor volumes, n=5-9 each group. Error bars mark standard deviation. **J)** Quantification of areas under curve (AUC) for overall tumor volumes from I). Error bars mark standard deviation. **K)** Two-way ANOVA analysis to compare weekly measured overall tumor volumes. Statistically significant p-values (<0.05) were highlighted in red. **L)** Representative images of IHC staining of H&E, ADAR1 (p150 isoform), and 4HNE in tumor samples resected from each treatment group. Scale bar, 200µm. See also **Figure S1**.

Figure 2: ADAR1 reduction leads to lipid remodeling

A) A simplified illustration highlighting key regulators of ferroptosis pathway. GSH, Glutathione. PL, phospholipid. MUFA, monounsaturated fatty acid. PUFA, polyunsaturated fatty acid. PM, plasma membrane. **B)** Heatmap of lipidomic analysis showed that ADAR1-knockdown results in lipid remodeling in MDA-MB-231 cells. PC, phosphatidylcholines. **C)** Relative abundance of PC species shown in B), listed in the order of carbon chain length. Values were log10 transformed, mean centered, and shown as mean over standard deviation ratio for each PC species. n=5. Red dots denote ADAR1-Intact (shNT), and blue dots denote ADAR1-Deficient (shADAR1) MDA-MB-231 samples. **D)** Relative abundance of PC species listed in the order of lipid unsaturation. n=5. **E)** Enrichment of PC species with different carbon chain lengths (28-30, 31-33, and >33 carbons) in ADAR1-Deficient over ADAR1-Intact MDA-MB-231 cells. **F)** Enrichment of PC species with different unsaturation levels (SFA, 0 double-bond; MUFA, 1 double-bond; PUFA, 2-3 double-bond; PUFA2, at least 4 double-bond) in ADAR1-Deficient over ADAR1-Intact MDA-MB-231 cells. **G)** Relative abundance of PC38:4 between ADAR1-Intact and -Deficient MDA-MB-231 cells. Left, detected peak intensity normalized to internal standard (ITSD). Right, log10 transformed and mean normalized peak intensity. n=5 **H)** Relative abundance of selected PC species in ADAR1-Intact and -Deficient MDA-MB-436 cells. Values were log10 transformed, mean centered, and shown as mean over standard deviation ratio. n=3. **I)** Relative abundance of PC44:6 between ADAR1-Intact and -Deficient MDA-MB-436 cells.

Detected peak intensity was log10 transformed and mean normalized. n=3. **J)** Relative abundance of PE and PS species in ADAR1-Intact and -Deficient MDA-MB-436 cells, listed in the order of lipid unsaturation. Values were log10 transformed, mean centered, and shown as mean over standard deviation ratio. n=3. **K)** Enrichment of PE and PS species with different unsaturation levels (MUFA, 1 double-bond; PUFA, 2-3 double-bond; PUFA2, at least 4 double-bond) in ADAR1-Deficient over ADAR1-Intact MDA-MB-436 cells. **L)** Relative abundance of PE38:5 between ADAR1-Intact and -Deficient MDA-MB-436 cells. Detected peak intensity was log10 transformed and mean normalized. n=3. See also **Figure S2**.

Figure 3: ADAR1 regulates MDM2 expression to dictate ferroptosis sensitivity

A) Venn diagram of significantly downregulated genes in ADAR1-Deficient over -Intact TNBC cell lines (MDA-MB-231, MDA-MB-468, HCC1806, BT549). **B)** Venn diagram of significantly upregulated genes in ADAR1-Deficient over -Intact TNBC cell lines (MDA-MB-231, MDA-MB-468, HCC1806, BT549). **C)** The ten most significantly altered signaling pathways (BioPlanet_2019) in ADAR1-Deficient over -Intact TNBC cell lines. Genes significantly altered (both up- and down-regulated) in at least 3 out of 4 cell lines tested are included in the analysis. **D)** The ten most significantly altered disease-related biological functions (PheWeb_2019) in ADAR1-Deficient over -Intact TNBC cell lines. Genes significantly altered in at least 3 out of 4 cell lines tested are included in the analysis. **E)** GSEA enrichment plot of ferroptosis related genes in ADAR1-Deficient MDA-MB-231 cells. **F)** GSEA enrichment plot of fatty acid metabolism genes in ADAR1-Deficient MDA-MB-231 cells. **G)** Venn diagram of the most significantly downregulated genes (log2<-0.4) in ADAR1-Deficient over -Intact TNBC cell lines. Genes altered in all 4 cell lines are listed on the right. **H)** Venn diagram of the most significantly upregulated genes (log2>0.4) in ADAR1-Deficient over -Intact TNBC cell lines. Genes altered in all 4 cell lines are listed on the right. **I)** Immunoblot analysis showed significant induction of MDM2 protein levels in ADAR1-Deficient (shADAR1) MDA-MB-231 cells. Images are representative of three replicates. GAPDH, loading control. **J)** Reported ADAR1 editing site (bolded and underlined) in MDM2 3'UTR. Numbers mark the location within MDM2 open reading frame. **K)** Reduced editing of MDM2 in ADAR1-Deficient TNBC cells. T/C were read with reverse primers in Sanger sequencing to indicate WT (T) and edited (C) RNA. Ratio of C/T peak heights indicates level of editing. Sequence chromatograms showed are representative of 3 independent experiments. **L)** Immunoblot analysis showed overexpression of MDM2 in MDA-MB-231 cells. Anti-MDM2 antibody detected both endogenous and overexpressed MDM2, and anti-Myc-tag antibody detected overexpressed MDM2 containing Myc-tag. GAPDH, loading control. ADAR1 level was not affected by MDM2 overexpression. **M)** Cell viability analysis was performed to determine IC_{50} values of ferroptosis inducers RSL3 for MDA-MB-231 cells with (MDM2) or without (Ctrl) MDM2 overexpression. Cell viability graph is representative of three independent experiments. FC, fold-change. **N)** Relative abundance of PUFA PC species, listed in the order of lipid unsaturation, in MDA-MB-231 cells with (red dots) or without (blue dots) MDM2 overexpression for 96 h. Values were log10 transformed, mean centered, and shown as mean over standard deviation ratio for each PC species. n=5. **O)** Relative abundance of PC42:7 between control (Ctrl) and MDM2-overexpressing MDA-MB-231 cells. Detected peak intensity was log10 transformed and mean

normalized. n=5. **P)** Relative cell viability within each of ADAR1-Intact (shNT) and -Deficient (shADAR1) MDA-MB-231 cells treated with RSL3 (100nM), as well as ADAR1-Deficient MDA-MB-231 cells co-treated with RSL3 and MDM2 inhibitors MX69 (10μM), MEL23 (10μM), and SP-141 (10μM), or PPAR-α agonist pirinixic acid (PA; 10μM) for 72h. n=3. Error bars mark standard error. See also **Figure S3 and Table S1-4**.

Figure 4: ADAR1 loss synergizes with cobimetinib to suppress tumorigenesis

A) Drug screen designed to identify ferroptosis modulators synergizing with ADAR1 loss. **B)** Anticipated results in identifying ADAR1-sensitized ferroptosis modulators. Small molecules (Exampled by blue dots) that display ADAR1-sensitized activity against cancer cells will reduce viability of ADAR1-Deficient (shADAR1) cells more strongly compared to ADAR1-Intact (shNT) cells. **C)** Screening result with a ferroptosis-focused library (654 small molecules) in MDA-MB-231 cells. X and Y axis represent cell viability for ADAR1-Intact (shNT) and -Deficient (shADAR1) cells after treatment, respectively. Data were normalized to cells treated with DMSO. RSL3 treatment was included as positive control for ADAR1-sensitized hits (red dots). Dashed line denotes expected locations for molecules without discriminating activity based on ADAR1 expression. **D)** Cell viability ratio of 0.51 (horizontal red line) between shADAR1 and shNT cells was used as the cutoff to identify ADAR1-sensitized hits (red dots). RSL3 treatment was included as positive control. **E)** List of hits identified from C) and D), ranked by cell viability ratio between treated shADAR1 and shNT MDA-MB-231 cells. **F)** Progression of overall tumor volumes throughout the treatment regimen, n=5-10 each group. Error bars mark standard deviation. **G)** Quantification of areas under curve (AUC) for overall tumor volumes from F). Error bars mark standard deviation. **H)** Two-way ANOVA analysis to compare weekly measured overall tumor volumes. Statistically significant p-values (<0.05) were highlighted in red. **I)** ADAR1 protects TNBC cells from ferroptosis through regulating MDM2 and lipid compositions between MUFA and PUFA. MUFA, monounsaturated fatty acid. PUFA, polyunsaturated fatty acid. FIN, ferroptosis inducer. See also **Figure S4**.

Figure S1. ADAR1 protects TNBC cells from ferroptosis induction

A) Immunoblot analysis showed significant reduction of ADAR1 protein levels in MDA-MB-231 cells treated with shADAR1-containing lentivirus. Images are representative of three replicates. GAPDH, loading control. **B)** Light and fluorescent images showed the morphology (Bright Field) and reduced and oxidized forms of the lipid peroxidation probe BODIPY^{TM} 581/591 C11 in ADAR1-Intact (shNT) and ADAR1-Deficient (shADAR1) MDA-MB-231 cells. **C)** Quantification of ratios of reduced over oxidized forms of BODIPY^{TM} 581/591 C11 in shNT and shADAR1 MDA-MB-231 cells. n=3. Error bars mark standard error. **D)** Concentration of the lipid peroxidation marker MDA in ADAR1-Intact and -Deficient MDA-MB-231 cells. n=3. Error bars mark standard deviation. **E)** Relative cell viability of ADAR1-Intact and -Deficient MDA-MB-231 cells, as well as ADAR1-Deficient MDA-MB-231 cells treated with apoptosis inhibitor Z-VAD-FMK (50μM), eIF2α inhibitor ISRIB (10μM), and ferroptosis inhibitors Fer-1 (Ferrostatin-1, 1μM) and Lip-1 (Liproxstatin-1, 1μM) for 72h. n=3 independent experiments. Error bars mark standard error. **F)** Light micrographs of MDA-MB-231 cells treated with RSL3 (10μM), in combination with DMSO, apoptosis inhibitor Z-VAD-FMK (5μM), necroptosis

inhibitor Nec-1 (Necrostatin-1, 5μM), and ferroptosis inhibitors Fer-1 (Ferrostatin-1, 5μM) and UAMC (5μM) for 24h. IC_{50} values of RSL3 were then determined for ADAR1-Intact and ADAR1-Deficient **G)** MCF7, **H)** ZR75.1, **I)** T47D and **J)** SKBR3 non-TNBC cells. Cell viability graphs are representatives of two independent experiments. **K)** Immunoblot analysis showed reduction of ADAR1 protein levels in lysates extracted from newly formed tumors from MDA-MB-231 cells possessing Tet-inducible shADAR1, 7 days after implanted mice (M1 and M2) were switched to doxycycline diet. GAPDH, loading control. **L)** Progression of average mouse weight between treatment groups, n=5-9 each group. Error bars mark standard deviation. **M)** Progression of relative tumor volumes, normalized to tumor volumes measured at week 0, throughout the treatment regimen, n=5-9 each group. Error bars mark standard deviation. **N)** Two-way ANOVA analysis compares weekly measured relative tumor volumes. Statistically significant p-values (<0.05) were highlighted in red. **O)** Representative images of tumors resected after the treatment regimens concluded. Scale bar, 5mm.

Figure S2: ADAR1 reduction leads to lipid remodeling

A) Concentration of Glutathione (GSH) in ADAR1-Intact (shNT) and -Deficient (shADAR1) MDA-MB-231 cells. n=3. Error bars mark standard deviation. **B)** Ratio of reduced/total levels of GSH to indicate GSH activity in ADAR1-Intact and -Deficient MDA-MB-231 cells. **C)** Light and fluorescent images showed the morphology (Bright Field) and ferrous ion detection (FerroOrange) in ADAR1-Intact and -Deficient MDA-MB-231 cells, respectively. **D)** Quantification of ferrous ion detection shown in C), normalized to cell numbers. n=3. Error bars mark standard error **E)** Significantly altered PC species (red dots) in ADAR1-Deficient compared to ADAR1-Intact MDA-MB-231 cells. PUFA PC species are marked. **F)** Immunoblot analysis showed significant reduction of ADAR1 protein levels in MDA-MB-436 cells treated with shADAR1-containing lentivirus. Images are representative of three replicates. GAPDH, loading control. **G)** Relative abundance of all detected PC species in ADAR1-Intact (red dots) and -Deficient (blue dots) MDA-MB-436 cells. Values were log10 transformed, mean centered, and shown as mean over standard deviation ratio. n=3. **H)** Relative abundance of PE and PS species in ADAR1-Intact and -Deficient MDA-MB-436 cells, listed in the order of carbon chain length. Values were log10 transformed, mean centered, and shown as mean over standard deviation ratio. n=3**. I)** Relative abundance of all detected PC, PE, and PS species in ADAR1-Intact and -Deficient MDA-MB-436 cells, listed in the order of lipid unsaturation. Values were log10 transformed, mean centered, and shown as mean over standard deviation ratio. n=3. Abundance of **J)** PC32:0, **K)** PC32:1, and **L)** PC34:1 positively correlate with *ADAR* (encoding ADAR1) expression level in TNBC (n=13), but not non-TNBC (n=23), cell lines. Data are extracted from publicly available metabolomics data set from DepMap (depmap.com).

Figure S3: ADAR1 regulates MDM2 expression to dictate ferroptosis sensitivity

A) RNA sequencing to identify significantly altered genes in ADAR1-Deficient TNBC cells. **B)** GeneOntology enrichment analysis for genes significantly altered in ADAR1-Deficient MDA-MB-231 cells, using PANTHER Overrepresentation Fisher's Exact Test. **C)** The ten most significantly altered biological pathways (Elsevier Collection Pathway) in ADAR1-Deficient over -Intact TNBC cell lines. Genes significantly altered (both up- and down-regulated) in at

least 3 out of 4 cell lines tested are included in the analysis. GSEA enrichment analyses were performed to assess regulated pathways such as **D)** Glutathione metabolism; **E)** Iron uptake and transport; **F)** Cell cycle; **G)** Interferon signaling; **H)** Glycolysis; **I)** Amino acid metabolism in ADAR1-Deficient MDA-MB-231 cells. **J)** Predicted RNA secondary structure of the entire MDM2 3'UTR and the reported ADAR1 editing site (circled in red in the zoomed-in square). **K)** RESS-qPCR showed that editing of MDM2 3'UTR site was reduced in ADAR1-Deficient MDA-MB-231 and MDA-MB-468 cells. n=3. Error bars mark standard error. **L)** Immunoblot analysis showed doxycycline-induced overexpression of MDM2 in MDA-MB-231 cells after 48 and 96 h. GAPDH, loading control. **M)** Relative abundance of PUFA PC species, listed in the order of lipid unsaturation, in MDA-MB-231 cells with (red dots) or without (blue dots) MDM2 overexpression for 48 h. Values were log10 transformed, mean centered, and shown as mean over standard deviation ratio for each PC species. n=5. **N)** Significantly enriched PUFA PC species (red dots) in MDM2-overexpressing (96h) compared to control MDA-MB-231 cells.

Figure S4: ADAR1 loss synergizes with cobimetinib to suppress tumorigenesis

A) Cobimetinib shows superior efficacy against TNBC (n=7) over non-TNBC (n=10) cell lines. Efficacy numbers (PRISM Repurposing Public 24Q2) <0 indicate reduced viability upon treatment. Data are extracted from publicly available data set from DepMap (depmap.com). **B)** Cobimetinib (TNBC: -0.72; non-TNBC: 0.71) shows superior preference, compared to carboplatin (TNBC: -0.75; non-TNBC: -0.18), against TNBC (n=7) over non-TNBC (n=10) cell lines. **C)** MDA-MB-231 cells (1.5 X 10^5 per mouse) possessing Tet-inducible shADAR1 were injected into mammary fat pads of female NSG mice through orthotopic implantations. Ten days post implantation, half of the mice were switched to doxycycline-containing (625mg/kg) diet. Two days after the diet switch, both control- and doxycycline-diet mice were subjected to cobimetinib treatments through oral administration (20mg/kg weight; twice a week) for 5 weeks before tumors were resected. **D)** Progression of average mouse weight between treatment groups, n=5-10 each group. Error bars mark standard deviation**. E)** Progression of relative tumor volumes, normalized to tumor volumes measured at week 0, throughout the treatment regimen, n=5-10 each group. Error bars mark standard deviation**. F)** Two-way ANOVA analysis to compare weekly measured relative tumor volumes. Statistically significant p-values (<0.05) were highlighted in red. **G)** Representative images of tumors resected after the treatment regimens concluded. Scale bar, 5mm. Drug sensitivity of TNBC, but not non-TNBC, cell lines to **H)** RSL3 (TNBC, n=9; non-TNBC, n=10), **I)** ML162 (TNBC, n=9; non-TNBC, n=11), and **J)** cobimetinib (TNBC, n=7; non-TNBC, n=7) negatively correlate with *ADAR* (encoding ADAR1) dependency (Chronos CRISPR Gene Effect). Lower AUC (RSL3, ML162) and efficacy (cobimetinib) numbers indicate higher drug sensitivity. Lower CRISPR Gene Effect numbers indicate higher *ADAR* dependency. Data are extracted from publicly available drug sensitivity (RSL3, ML162: Drug sensitivity AUC, CTD[2]; cobimetinib: PRISM Repurposing Public 24Q2) and gene dependency (Public 24Q2+Score, Chronos) data sets from DepMap (depmap.com).

Figure 1

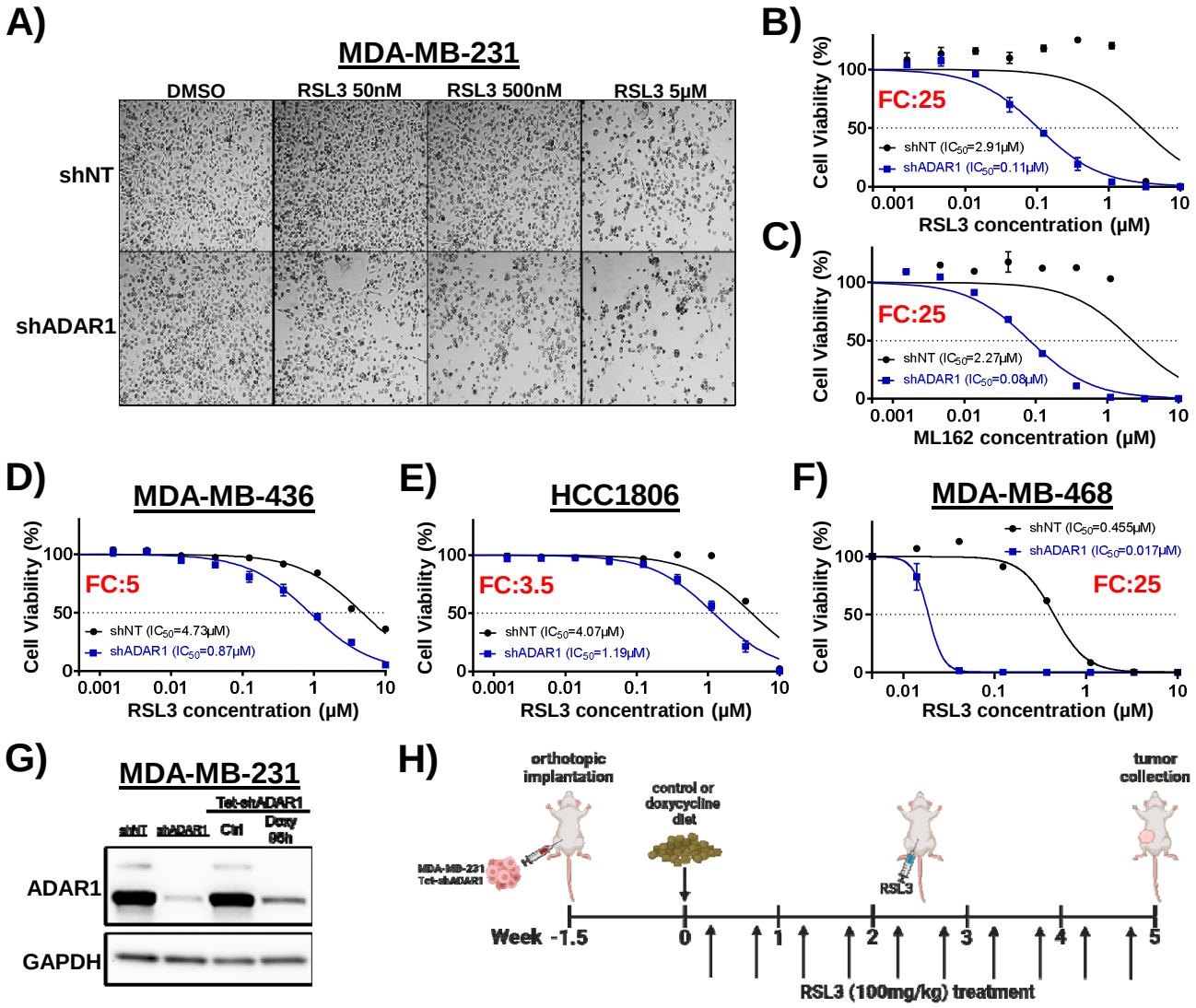

Comparison		p-Value - Post Treatment (Week)					
Group 1	Group 2	0	1	2	3	4	5
Ctrl - Ctrl	Doxy - Ctrl	>0.999	0.957	0.367	0.015	<0.0001	<0.0001
Ctrl - Ctrl	Ctrl - RSL3	>0.999	0.984	0.472	0.005	<0.0001	<0.0001
Ctrl - Ctrl	Doxy - RSL3	>0.999	0.836	0.087	<0.0001	<0.0001	<0.0001
Doxy - Ctrl	Doxy - RSL3	>0.999	0.999	0.963	0.234	0.059	<0.0001
Ctrl - RSL3	Doxy - RSL3	>0.999	0.997	0.964	0.606	0.120	0.002

Figure 2

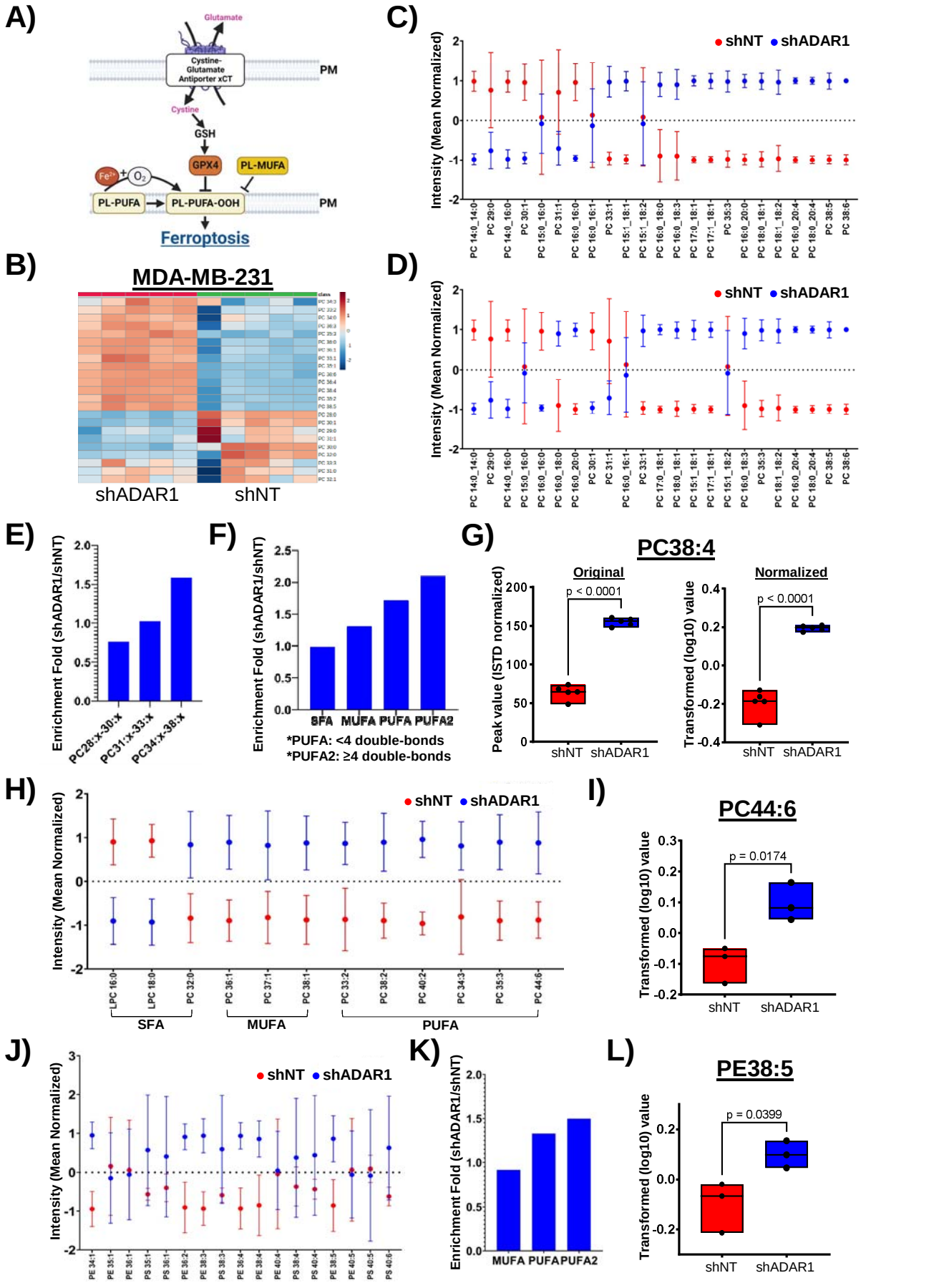
A)
Glutamate
Cystine-Glutamate Antiporter xCT
PM
Cystine
GSH
GPX4
PL-MUFA
PL-PUFA
PL-PUFA-OOH
PM
Ferroptosis
B)
MDA-MB-231
shADAR1
shNT
C)
shNT shADAR1
Intensity (Mean Normalized)
D)
shNT shADAR1
Intensity (Mean Normalized)
E)
Enrichment Fold (shADAR1/shNT)
PC28:x-30:x
PC31:x-33:x
PC34:x-38:x
F)
Enrichment Fold (shADAR1/shNT)
SFA MUFA PUFA PUFA2
*PUFA: <4 double-bonds
*PUFA2: ≥4 double-bonds
G)
PC38:4
Original
Normalized
p < 0.0001
p < 0.0001
Peak value (ISTD normalized)
Transformed (log10) value
shNT shADAR1
H)
shNT shADAR1
Intensity (Mean Normalized)
SFA
MUFA
PUFA
I)
PC44:6
p = 0.0174
Transformed (log10) value
shNT shADAR1
J)
shNT shADAR1
Intensity (Mean Normalized)
K)
Enrichment Fold (shADAR1/shNT)
MUFA PUFA PUFA2
L)
PE38:5
p = 0.0399
Transformed (log10) value
shNT shADAR1

Figure 3

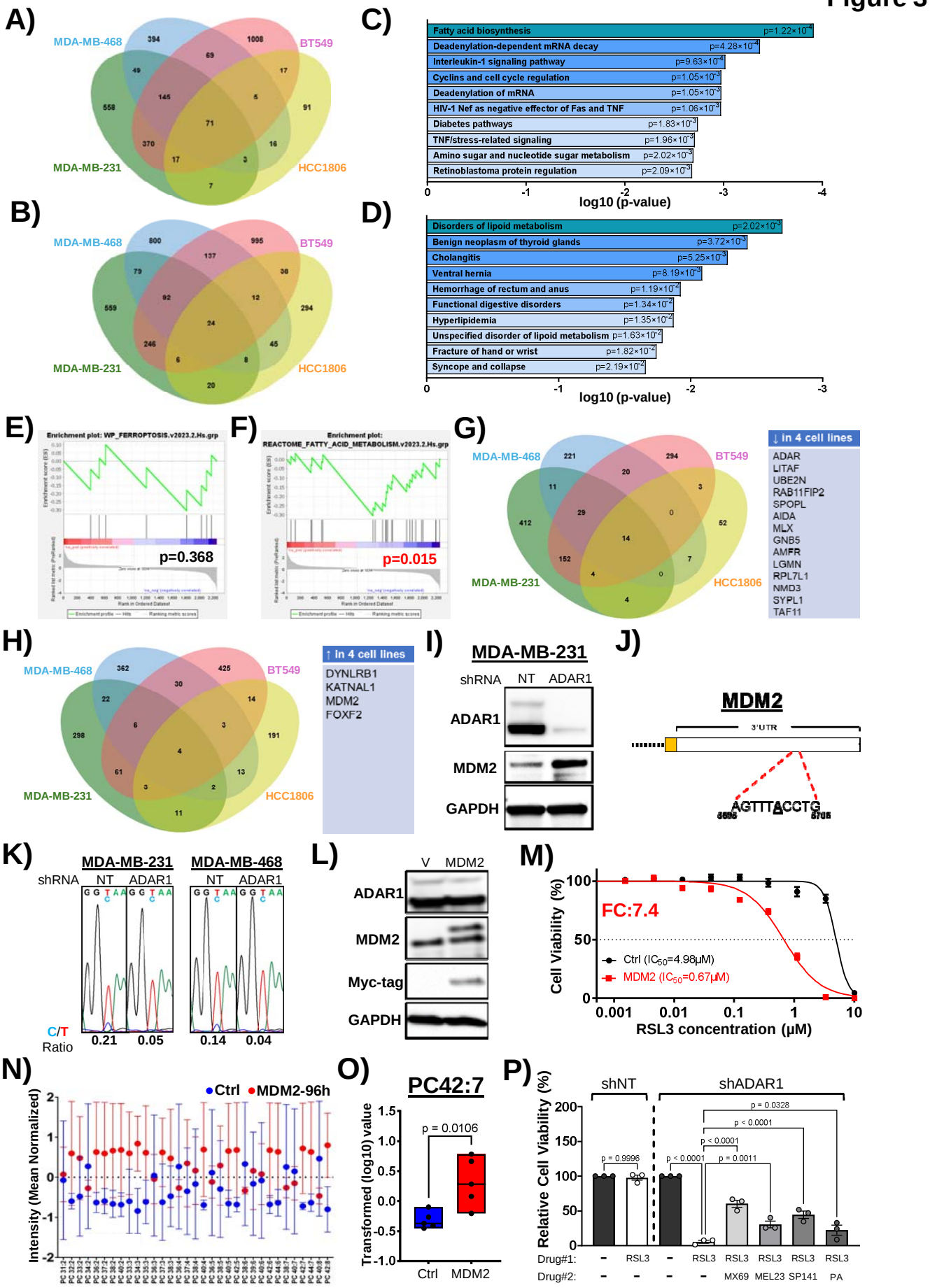
A)
MDA-MB-468
BT549
MDA-MB-231
HCC1806
394
1008
69
49
17
558
145
5
91
71
370
16
17
3
7
B)
MDA-MB-468
BT549
MDA-MB-231
HCC1806
800
995
137
79
38
559
92
12
294
24
246
45
6
8
20
C)
Fatty acid biosynthesis p=1.22×10-4
Deadenylation-dependent mRNA decay p=4.28×10-4
Interleukin-1 signaling pathway p=9.63×10-4
Cyclins and cell cycle regulation p=1.05×10-3
Deadenylation of mRNA p=1.05×10-3
HIV-1 Nef as negative effector of Fas and TNF p=1.06×10-3
Diabetes pathways p=1.83×10-3
TNF/stress-related signaling p=1.96×10-3
Amino sugar and nucleotide sugar metabolism p=2.02×10-3
Retinoblastoma protein regulation p=2.09×10-3
0 -1 -2 -3 -4
log10 (p-value)
D)
Disorders of lipoid metabolism p=2.02×10-3
Benign neoplasm of thyroid glands p=3.72×10-3
Cholangitis p=5.25×10-3
Ventral hernia p=8.19×10-3
Hemorrhage of rectum and anus p=1.19×10-2
Functional digestive disorders p=1.34×10-2
Hyperlipidemia p=1.35×10-2
Unspecified disorder of lipoid metabolism p=1.63×10-2
Fracture of hand or wrist p=1.82×10-2
Syncope and collapse p=2.19×10-2
0 -1 -2 -3
log10 (p-value)
E)
Enrichment plot: WP_FERROPTOSIS.v2023.2.Hs.grp
p=0.368
F)
Enrichment plot: REACTOME_FATTY_ACID_METABOLISM.v2023.2.Hs.grp
p=0.015
G)
MDA-MB-468
BT549
MDA-MB-231
HCC1806
221
294
20
11
3
29
0
412
52
14
152
7
4
0
4
↓ in 4 cell lines
ADAR
LITAF
UBE2N
RAB11FIP2
SPOPL
AIDA
MLX
GNB5
AMFR
LGMN
RPL7L1
NMD3
SYPL1
TAF11
H)
MDA-MB-468
BT549
MDA-MB-231
HCC1806
362
425
30
22
14
6
298
3
191
4
61
13
3
2
11
↑ in 4 cell lines
DYNLRB1
KATNAL1
MDM2
FOXF2
I)
MDA-MB-231
shRNA NT ADAR1
ADAR1
MDM2
GAPDH
J)
MDM2
3'UTR
AGTTTACCTG
5695 5705
K)
MDA-MB-231
MDA-MB-468
shRNA NT ADAR1 NT ADAR1
C/T Ratio
0.21 0.05 0.14 0.04
L)
V MDM2
ADAR1
MDM2
Myc-tag
GAPDH
M)
FC:7.4
Ctrl (IC50=4.98μM)
MDM2 (IC50=0.67μM)
Cell Viability (%)
100
50
0
0.001 0.01 0.1 1 10
RSL3 concentration (μM)
N)
Ctrl MDM2-96h
Intensity (Mean Normalized)
2 1 0 -1 -2
O)
PC42:7
p = 0.0106
Transformed (log10) value
1.5 1.0 0.5 0.0 -0.5 -1.0
Ctrl MDM2
P)
shNT shADAR1
Relative Cell Viability (%)
200 150 100 50 0
p = 0.9996
p < 0.0001
p = 0.0011
p < 0.0001
p < 0.0001
p = 0.0328
Drug#1: - RSL3 - RSL3 RSL3 RSL3 RSL3 RSL3
Drug#2: - - - - MX69 MEL23 SP141 PA

Figure 4

A)

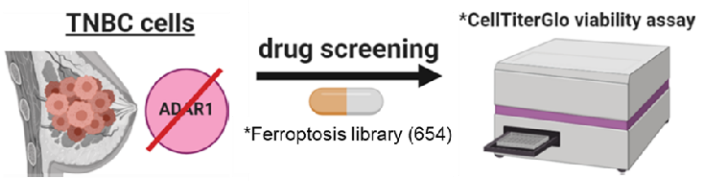

B)

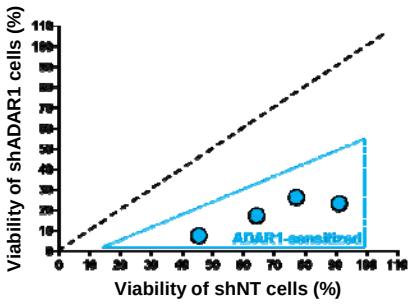

C)

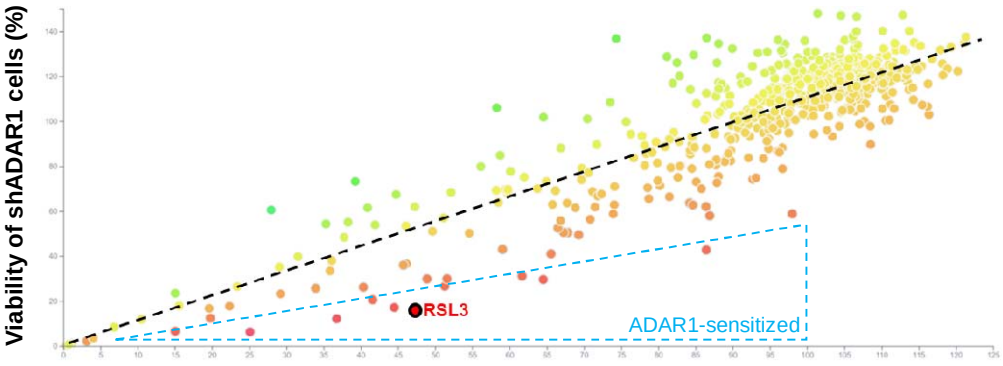

D)

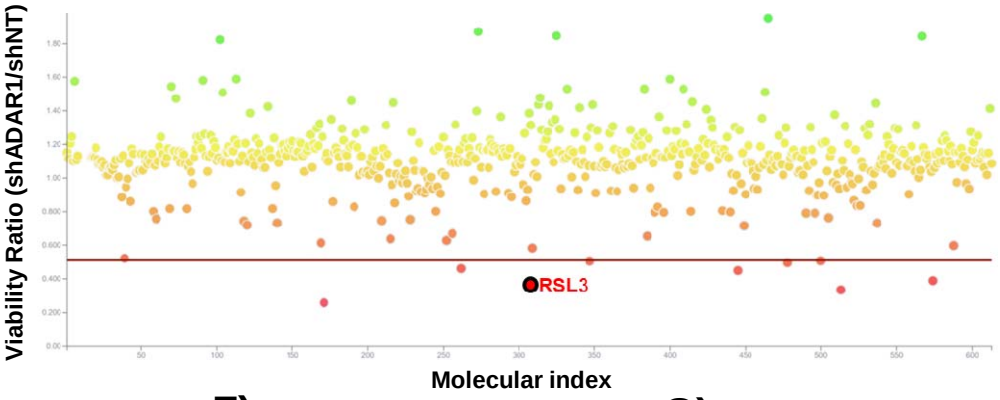

E)

Drug	Viability Ratio (shADAR1/shNT)
Siramesine	0.26
SB-590885	0.33
α-Mangostin	0.39
GW284543	0.45
UC2288	0.46
Nordihydroguaiaretic acid (NDGA)	0.5
Cobimetinib	0.51
Cobimetinib (racemate)	0.51

F)

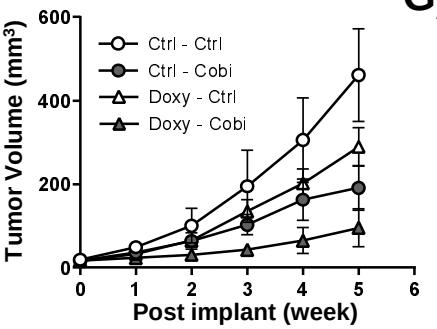

G)

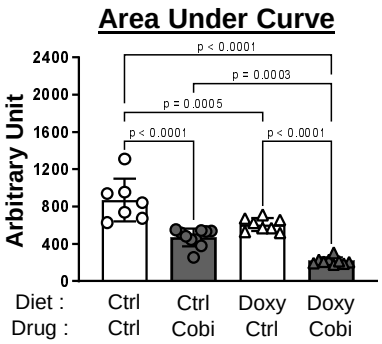

H)

Comparison		p-Value - Post Treatment (Week)					
Group 1	Group 2	0	1	2	3	4	5
Ctrl - Ctrl	Doxy - Ctrl	>0.999	0.957	0.367	0.015	<0.0001	<0.0001
Ctrl - Ctrl	Ctrl - Cobi	>0.999	0.979	0.319	<0.0001	<0.0001	<0.0001
Ctrl - Ctrl	Doxy - Cobi	>0.999	0.725	0.002	<0.0001	<0.0001	<0.0001
Doxy - Ctrl	Doxy - Cobi	>0.999	0.994	0.436	<0.0001	<0.0001	<0.0001
Ctrl - Cobi	Doxy - Cobi	>0.999	0.980	0.426	0.011	<0.0001	<0.0001
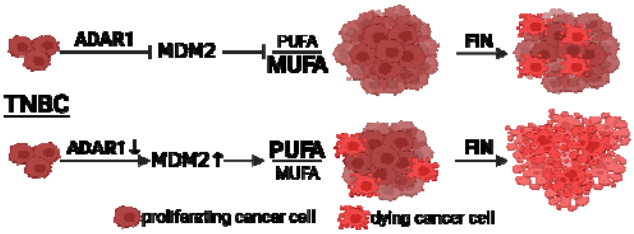
I)